Flow topology and enstrophy production in chemically reacting compressible isotropic turbulence

Jian Teng, Jianchun Wang,* and Shiyi Chen
Department of Mechanics and Aerospace Engineering, Southern University of Science and Technology, Shenzhen 518055, China;
Southern Marine Science and Engineering Guangdong Laboratory (Guangzhou), Guangzhou 511458, China; and Guangdong-Hong Kong-Macao Joint Laboratory for Data-Driven Fluid Mechanics and Engineering Applications, Southern University of Science and Technology, Shenzhen 518055, China

(Received 10 December 2020; accepted 8 March 2022; published 31 March 2022)

Flow topology and enstrophy production in chemically reacting compressible isotropic turbulence are studied by using numerical simulations with solenoidal forcing at initial turbulent Mach numbers ranging from 0.2 to 0.6 and at initial Taylor Reynolds numbers ranging from 32 to 160. A detailed chemical kinetic mechanism including nine species and 19 elementary reactions is employed to represent the H_2/O_2 reaction in turbulence. It is found that heat release leads to an increase of internal energy and turbulent length scales. After strong heat release during the chemical reaction process, the instantly increased temperature results in the increase of viscosity and pressure work, leading to the decrease of turbulent Mach number and Taylor Reynolds number, as well as the decrease of intrinsic flow compressibility and density gradient magnitude. Various statistical properties of eight flow topologies based on the three invariants of velocity gradient tensor are investigated with a specific focus on the effect of reaction heat release and compressibility. The topologies unstable focus/compressing (UFC), unstable node/saddle/saddle (UN/S/S), and stable focus/stretching (SFS) are predominant flow patterns at three turbulent Mach numbers. The topologies UN/S/S and SFS have major contributions to the overall enstrophy production in expansion regions, while the topology UFC leads to evident destruction of enstrophy in compression regions. The strong compression motions cause the destruction of enstrophy by the interaction between the vorticity and strain rate tensor, while strong expansion motions significantly enhance the generation of enstrophy. The most probable eigenvalue ratios for the strain rate tensor at three turbulent Mach numbers are found to be −4:1:3 in the overall flow field. Overall, the heat release by chemical reaction significantly reduces the compressibility effect on the local flow topologies and enstrophy production in chemically reacting compressible turbulence.

DOI: 10.1103/PhysRevFluids.7.033201

I. INTRODUCTION

In turbulent flows, the chaotic small-scale turbulent motions can be studied conveniently by examining the behaviors of flow quantities in different flow topologies. Chong *et al*. [1] proposed a general classification of three-dimensional flow patterns based on the invariants of the velocity gradient tensor. For incompressible turbulence, the first invariant of the velocity gradient tensor is zero due to the continuity condition. Thus, the local flow topologies can be characterized by the two-dimensional plane of the second and third invariants of the velocity gradient tensor. It was

*Corresponding author: wangjc@sustech.edu.cn

observed that the joint probability density function (PDF) of the second and third invariants of the velocity gradient tensor exhibits a universal "teardrop" shape with a statistical preference in the second and fourth quadrants, and the corresponding local topologies unstable node/saddle/saddle and stable focus/stretching are predominant in a wide variety of incompressible turbulence [2–6]. The flow topology in compressible turbulence is more complex, as compared to that of incompressible turbulence. There are nonlinear couplings of the solenoidal mode, compressible mode and thermodynamic mode for compressible turbulence, leading to the distinct flow structures and statistical features of velocity field in compressible turbulence [7–13].

Enstrophy is an important quantity which characterizes the rotation of small-scale motions in turbulent flows [14]. Vortex stretching, which results from nonlinear coupling between vorticity and strain rate tensor, is a characteristic feature of turbulence and is responsible for transporting velocity fluctuations over different length scales [15,16]. The alignment of the vorticity vector and the second eigenvector of the strain rate tensor has a tendency to be positive on average, and thus leads to the production of enstrophy in turbulent flows [6,17–20]. Understanding of enstrophy production is important to reveal many complex phenomena in turbulence, including energy cascade, material element deformation, and small-scale motions [21]. Tsinober [22] examined the statistical relation between strain production and enstrophy production of wall-bounded flows in the invariant map of the second and third invariants of velocity gradient tensor and concluded that nonlinearities prevails in the fourth quadrant of the invariant map of the second and third invariants of velocity gradient tensor, in which the production of strain predominates over enstrophy production. Bechlars *et al*. [23] studied the compressible evolution equations for three invariants of the velocity gradient tensor and the probability distribution of the enstrophy production in the compressible turbulent boundary layer. They found that even though the ratio of the principal strains and the alignment of vorticity with the eigenvectors of the strain rate tensor varies with the wall distance in the boundary layer, the enstrophy production exhibits self-similarity above the buffer layer. The discussion of enstrophy production in different flow topologies is more convenient to reveal the local behaviors of small-scale motions in compressible turbulence. Wang *et al*. [24] studied the flow topologies in compressible turbulent boundary layers and observed that enstrophy production relies on the topology unstable node/saddle/saddle in the inner layer and on the topology unstable focus/stretching in the outer layer.

In chemically reacting turbulence, the swirl motion and strain can strongly affect local scalar structure and species mixing [25]. Moreover, heat release through chemical reactions can affect small-scale flow motions and change the statistics of the enstrophy production and thermochemical transport [26]. Tanahashi *et al*. [27] analyzed the direct numerical simulation (DNS) database of a hydrogen/air turbulent premixed flame and used the second invariant of the velocity gradient tensor to distinguish strain-dominated and vorticity-dominated regions. They found that the vorticity vector remains perpendicular to the flame normal vector and the coherent structures can survive beyond the flame front. Cifuentes *et al*. [28] investigated the statistical properties of various flow topologies in turbulent premixed flames and found that the universal teardrop shape of the joint PDF of the second and third invariants of the velocity gradient tensor disappears in the "fresh reactant" region. Wacks *et al*. [29] studied the statistics of local flow topologies and velocity gradient as well as their influence on the scalar dissipation rate and enstrophy transport in turbulent premixed flames. They also examined the sensitivity of the joint PDF of the second and third invariants of the velocity gradient tensor to the Lewis number. The effect of local flow topology on the enstrophy transport was further analyzed in different regimes of the premixed turbulent combustion field, including the corrugated flamelets, thin reaction zones, and broken reaction zones [26].

For highly compressible chemically reacting turbulence, the compressibility effect and reaction heat release further complicate the behavior of small-scale motions. Wang *et al*. [30] studied the compressibility effects on small-scale structure by analyzing a DNS database of nonreacting compressible isotropic turbulence at turbulent Mach number around 1.0 and found that the enstrophy production highly depends on the local flow dilatation. They demonstrated that strong local compression motions enhance the enstrophy production by vortex stretching, while strong

local expansion motions suppress enstrophy production by vortex stretching. The presence of shocklets in highly compressible turbulence considerably increases flow dilatation at small scales, which significantly enhances enstrophy production. Thus, analysis of enstrophy production and transportation is essential for understanding the small-scale flow behaviors and flame structures in combusting turbulence [26,31,32]. Nevertheless, the combined effects of heat release through chemical reactions and turbulence compressibility on flow topology as well as enstrophy production in compressible chemically reacting turbulence are less understood.

The current study aims to explore flow topology of small-scale motions in solenoidally forced chemically reacting compressible isotropic turbulence at initial turbulent Mach numbers ranging from 0.2 to 0.6 and at initial Taylor Reynolds numbers ranging from 32 to 160, with a specific focus on the effects of reaction heat release and compressibility on various flow topologies. In-depth analysis is carried out on the enstrophy production at various flow topologies. The rest of the paper is organized as follows. In Sec. II the governing equations are presented and the numerical methodology is elaborated. The reaction process and one-point statistics of the simulated reactive flows are presented in Sec. III. The statistical properties of the flow topology and its influence on enstrophy production are discussed in Sec. IV. A summary of major findings and conclusions are provided in Sec. V.

II. GOVERNING EQUATIONS AND NUMERICAL STRATEGY

Numerical simulations of solenoidally forced stationary chemically reacting compressible turbulence are performed, employing the following dimensionless Navier-Stokes equations [33–35] in conservative form:

$$\frac{\partial \rho}{\partial t} + \frac{\partial(\rho u_j)}{\partial x_j} = 0, \tag{1}$$

$$\frac{\partial(\rho u_i)}{\partial t} + \frac{\partial(\rho u_i u_j + p\delta_{ij})}{\partial x_j} = \frac{1}{\mathrm{Re}}\frac{\partial \sigma_{ij}}{\partial x_j} + \mathcal{F}_i, \tag{2}$$

$$\frac{\partial \mathcal{E}}{\partial t} + \frac{\partial[(\mathcal{E}+p)u_j]}{\partial x_j} = \frac{1}{\alpha}\frac{\partial}{\partial x_j}\left(\kappa\frac{\partial T}{\partial x_j}\right) + \frac{1}{\mathrm{Re}}\frac{\partial(\sigma_{ij}u_i)}{\partial x_j} + \Theta - \Lambda + \mathcal{F}_j u_j, \tag{3}$$

$$\frac{\partial(\rho Y_s)}{\partial t} + \frac{\partial(\rho Y_s u_j)}{\partial x_j} = \frac{1}{\mathrm{Re}}\frac{1}{\mathrm{Sc}_s}\frac{\partial}{\partial x_j}\left(\mu\frac{\partial Y_s}{\partial x_j}\right) + \dot{\omega}_s,\ s = 1, 2, \ldots, n_s - 1, \tag{4}$$

$$p = \rho T/(\gamma M^2 \mathbb{M}), \tag{5}$$

where u_i is the velocity component, p is the pressure, T is the temperature, ρ is the mixture density, and $\mathbb{M}$ is the mean molecular weight of the mixture, where $\mathbb{M} = 1/\sum_{s=1}^{n_s}(Y_s/\mathbb{M}_s)$, Y_s, and $\mathbb{M}_s$ denote mass fraction and dimensionless molecular weight of the sth species, respectively. n_s is the total number of species. The viscous stress σ_{ij} is given by

$$\sigma_{ij} = \mu\left(\frac{\partial u_i}{\partial x_j} + \frac{\partial u_j}{\partial x_i}\right) - \frac{2}{3}\mu\theta\delta_{ij}, \tag{6}$$

where $\theta = \partial u_k/\partial x_k$ is the velocity divergence. For the multispecies mixture, $\dot{\omega}_s$ is the sth species production rate. Θ denotes total heat of reaction, where $\Theta = -\sum_{s=1}^{n_s} H_s^0\dot{\omega}_s/[(\gamma-1)M^2]$ and $-H_s^0$ is the dimensionless heat of reaction for sth species. [33,35].

The total energy per unit volume $\mathcal{E}$ is defined by

$$\mathcal{E} = \frac{p}{\gamma - 1} + \frac{1}{2}\rho(u_j u_j). \tag{7}$$

A set of reference scales are used to normalize the variables in chemically reacting compressible turbulence, including the reference length L_f, velocity U_f, density ρ_f, pressure $p_f = \rho_f U_f^2$, temperature T_f, energy per unit volume $\rho_f U_f^2$, species source term $\rho_f U_f/L_f$, heat of reaction

$C_{p,f}T_f$, molecular weight $\mathbb{M}_f$, viscosity μ_f, and thermal conductivity κ_f. Three reference governing parameters are derived: the reference Reynolds number $\mathrm{Re} = \rho_f U_f L_f/\mu_f$, the reference Mach number $M = U_f/c_f$, and the reference Prandtl number $\mathrm{Pr} = \mu_f C_{p,f}/\kappa_f$. The speed of sound is defined by $c_f = \sqrt{\gamma R_f T_f}$, where R_f is the specific gas constant and $\gamma = C_{p,f}/C_{v,f}$ is the ratio of specific heat at constant pressure $C_{p,f}$ to that at constant volume $C_{v,f}$. γ is assumed to be equal to 1.4 in our simulations. The parameter α is defined by $\alpha = \mathrm{Pr}\,\mathrm{Re}(\gamma-1)M^2$. It is assumed that the parameter $\mathrm{Pr} = 0.7$ and the gas is perfect [33,36].

Sutherland's law is adopted for calculation of the nondimensional temperature-dependent viscosity coefficient μ and thermal conductivity coefficient κ [37]:

$$\mu = \frac{1.4042T^{1.5}}{T + 0.40417}, \tag{8}$$

$$\kappa = \frac{1.4042T^{1.5}}{T + 0.40417}. \tag{9}$$

For the convenience of subsequent discussions, the governing equations for kinetic energy $\mathcal{E}_K$ and internal energy $\mathcal{E}_I$ are given by [37–40]

$$\frac{\partial \mathcal{E}_K}{\partial t} + \frac{\partial(\mathcal{E}_K u_j)}{\partial x_j} + \frac{\partial(pu_j)}{\partial x_j} - \frac{1}{\mathrm{Re}}\frac{\partial(\sigma_{ij}u_i)}{\partial x_j} = p\theta - \frac{1}{\mathrm{Re}}\sigma_{ij}\frac{\partial u_i}{\partial x_j} + \mathcal{F}_j u_j, \tag{10}$$

$$\frac{\partial \mathcal{E}_I}{\partial t} + \frac{\partial(\mathcal{E}_I u_j)}{\partial x_j} = -p\theta + \frac{1}{\alpha}\frac{\partial}{\partial x_j}\left(\kappa\frac{\partial T}{\partial x_j}\right) + \frac{1}{\mathrm{Re}}\sigma_{ij}\frac{\partial u_i}{\partial x_j} + \Theta - \Lambda, \tag{11}$$

where $\mathcal{E}_K = \rho u_j u_j/2$ and $\mathcal{E}_I = \rho T/[(\gamma-1)\gamma M^2]$. Terms on the right-hand side of Eq. (10) represent work due to pressure-dilatation, viscous stress, and the energy injection through forcing, while terms on the right-hand side of Eq. (11) represent pressure-dilatation work, heat diffusion, viscous dissipation, reaction heat release, and the cooling rate. For homogeneous isotropic turbulence with periodic boundary conditions, applying the spatial average operation $\langle\cdot\rangle$ over the entire domain gives

$$\frac{\partial\langle\mathcal{E}_K\rangle}{\partial t} = \langle p\theta\rangle - \frac{1}{\mathrm{Re}}\left\langle\sigma_{ij}\frac{\partial u_i}{\partial x_j}\right\rangle + \langle\mathcal{F}_j u_j\rangle, \tag{12}$$

$$\frac{\partial\langle\mathcal{E}_I\rangle}{\partial t} = -\langle p\theta\rangle + \frac{1}{\mathrm{Re}}\left\langle\sigma_{ij}\frac{\partial u_i}{\partial x_j}\right\rangle + \langle\Theta\rangle - \langle\Lambda\rangle. \tag{13}$$

The large-scale forcing $\mathcal{F}_i$ is applied to the solenoidal velocity component by fixing the velocity spectrum within the two lowest wave number shells [9,37,41]. The effect of the spatially uniform cooling function Λ in the energy conservation equation is to partly remove internal energy, in order to balance the energy injection through the large-scale forcing. We have considered the following cooling function:

$$\Lambda = \sigma T^m, \tag{14}$$

where $m = 0$. Previous studies showed that the results are not sensitive to the type of cooling applied for $m = 0$, 2 and 4. In the wave number space, the essential dynamics of energy transfer involves kinetic energy transfer from large to small scales through a forward kinetic energy cascade and the viscous dissipation process converting local kinetic energy to internal energy. For statistically stationary flow without chemical reaction heat release, there is $\overline{\langle\mathcal{F}_j u_j\rangle} - \overline{\langle\Lambda\rangle} = 0$, where the overline represents the time average [37]. This equation precisely expresses the relation between kinetic energy injection and the cooling function in the energy conservation equation. In other words, the large-scale forcing $\mathcal{F}_j$, which maintains the forward kinetic energy cascade from large to small scales, and the cooling function, which removes the increased internal energy due to viscous dissipation constitute a total energy conservation system. The averaged internal energy per unit volume is given by $E_I = \langle\mathcal{E}_I\rangle$. In the programming for numerical simulations without chemical reaction heat release, the cooling function keeps the total energy constant at each time step by

ensuring $\langle \rho T \rangle^{(n)} = \langle \rho T \rangle^{(initial)}$, where the superscripts (n) and $(initial)$ represent the value at the nth time step and the initial value after initialization, respectively. For the situation with chemical reaction heat release, the cooling function keeps the total energy in a new step to be equal to total energy in the previous step plus the total heat release by a chemical reaction by ensuring $\langle \rho T \rangle^{(n+1)} = \langle \rho T \rangle^{(n)} + \langle \Theta \rangle dt$, where the superscript (n) denotes a value in the current time step, $(n+1)$ represents a value in the next time step, and dt is the time step size.

The H_2/O_2 reaction that includes 19 elementary reactions and nine species is used in current simulations [42]. The species are H, H_2, O, O_2, OH, H_2O, HO_2, H_2O_2, and N_2. The Schmidt number for each species is determined by the Lewis number [43] as follows where $\mathrm{Sc}_s = \mathrm{Le}_s \mathrm{Pr}$:

$$\mathrm{Le}_{H_2} = 0.3, \quad \mathrm{Le}_{O_2} = 1.11, \quad \mathrm{Le}_{O} = 0.7, \quad \mathrm{Le}_{OH} = 0.73, \tag{15}$$

$$\mathrm{Le}_{H_2O} = 0.83, \quad \mathrm{Le}_{H} = 0.18, \quad \mathrm{Le}_{HO_2} = 1.10, \quad \mathrm{Le}_{H_2O_2} = 1.12. \tag{16}$$

Calculation of chemical reaction parameters is based on dimensional variables, which are denoted by the superscript "D." The detailed chemical reaction kinetic mechanism is given by Li *et al*. [42]. The general finite rate reaction equation is written as

$$\sum_{s=1}^{n_s} v'_{s,r} \chi_s \underset{K_{b,r}}{\overset{K_{f,r}}{\rightleftharpoons}} \sum_{s=1}^{n_s} v''_{s,r} \chi_s, \quad r = 1, 2, \ldots, n_r, \tag{17}$$

where χ_s is the mole fraction of sth species, $v'_{s,r}$, $v''_{s,r}$ represent the stoichiometric mole numbers of the reactants and products, and $K_{f,r}$, $K_{b,r}$ represent the forward and backward reaction rate coefficient for the rth elementary reaction, respectively. Both the forward and backward reaction rate coefficients of rth reaction can be calculated with the Arrhenius equation [42] as follows:

$$K_r = A_r T^{B_r} e^{-C_r/\mathbb{R}T^D}, \tag{18}$$

where A_r, B_r, and C_r are found from experimental data and $\mathbb{R}$ is the universal gas constant. The dimensional source term of of sth species $\dot{\omega}_s^D$ can be calculated by

$$\dot{\omega}_s^D = \mathbb{M}_s^D \sum_{r=1}^{n_r} \left[(v''_{s,r} - v'_{s,r}) \left(K_{f,r} \prod_{s=1}^{n_s} \chi_s^{v'_{s,r}} - K_{b,r} \prod_{s=1}^{n_s} \chi_s^{v''_{s,r}} \right) \right]. \tag{19}$$

The dimensional source term $\dot{\omega}_s^D$ and heat of reaction $-H_s^{0,D}$ of sth species are nondimensionalized as $\dot{\omega}_s = \dot{\omega}_s^D / [\rho_f (U_f / L_f)]$ and $-H_s^0 = -H_s^{0,D} / (C_{p,f} T_f)$, respectively. To validate the chemical modeling, a zero-dimensional chemical reaction model is derived in Appendix A. The good agreement of experimental data with results obtained by the current adopted method for the species source terms and heat of reaction suggests that the chemical modeling is valid.

The governing equations of chemically reacting compressible turbulence are solved numerically in a cubic domain of $(2\pi)^3$ by using periodic boundary conditions in all three spatial directions. A hybrid scheme combining an eighth-order compact finite difference scheme for smooth regions [44] and a seventh-order weighted essentially nonoscillatory (WENO) scheme [45,46] for shock regions [30,37,47,48] is adopted for both weakly and highly compressible reacting isotropic turbulence. To implement the shock detecting process, a shock front detecting relation $\theta < -R_\theta \theta'$ [7] is used, where $R_\theta = 3.0$. Then the shock front and additional six grid points on both the left and right in each spatial direction immediately outside the shock front are treated as a shock region that is calculated with the WENO scheme. The remaining region is treated as the smooth region [37]. Successful applications of this numerical scheme are seen in [12,21,30,38,40,49–52].

III. REACTION PROCESS AND SIMULATION STATISTICS

The entire simulation process includes two consecutive steps. In the first step, an inert flow is simulated where the species evolve with turbulent motions through diffusion and advection

without chemical reaction. In the second step, the chemical reaction is activated when the flow is fully developed. The initial pressure and temperature of the reacting mixture are 32 424 Pa and 880 K, respectively. The initial mole fraction for species H_2, O_2, and N_2 are 0.16, 0.08, and 0.76, respectively. Initial mole fractions for the other six species in the mixture are assigned to 0.0. The Taylor microscale Reynolds number Re_λ and the turbulent Mach number M_t are defined, respectively by [37,47]

$$\mathrm{Re}_\lambda = \mathrm{Re}\frac{\langle\rho\rangle u'\lambda}{\sqrt{3}\langle\mu\rangle}, \quad M_t = M\frac{u'}{\langle\sqrt{T}\rangle}, \tag{20}$$

where $\langle\cdot\rangle$ stands for spatial average and the Taylor microscale is

$$\lambda = \sqrt{\frac{\langle u_1^2 + u_2^2 + u_3^2\rangle}{\langle(\partial u_1/\partial x_1)^2 + (\partial u_2/\partial x_2)^2 + (\partial u_3/\partial x_3)^2\rangle}}. \tag{21}$$

Three sets of a grid (64^3, 128^3, 256^3) are employed for numerical simulations at initial Taylor Reynolds numbers 32, 64, and 160, respectively. The initial turbulent Mach numbers for each grid resolution are assigned to 0.2, 0.4, and 0.6. The nondimensional initial temperature is 1.0. The nondimensional initial pressure is 92, 23, and 10 for initial turbulent Mach numbers 0.2, 0.4, and 0.6, respectively.

To present a general view of the chemical reaction process, the temporal variations of flow statistics in the simulated data with 256^3 grid resolution for three initial turbulent Mach numbers are shown in Fig. 1. The chemical reaction time t is normalized by the large-eddy turnover time τ, where $\tau = L_I/u'$. The normalization can be used to assess the overall chemical reaction timescale relative to the characteristic turbulent timescale. Here L_I is the integral length scale defined by

$$L_I = \frac{3\pi}{2(u')^2}\int_0^\infty \frac{E(k)}{k}\,dk, \tag{22}$$

where $E(k)$ is the spectrum of kinetic energy per unit mass, namely, $\int_0^\infty E(k)\,dk = (u')^2/2$. $u' = \sqrt{\langle u_1^2 + u_2^2 + u_3^2\rangle}$ is the root-mean-squared (r.m.s.) velocity magnitude. In Fig. 1 the start point $t/\tau = 0$ represents the end of inert flow simulation and the activation of the chemical reaction. The temporal variations of spatial average of normalized heat release $\langle\Theta\rangle(\gamma-1)M^2$ and spatially averaged temperature $\langle T\rangle$ are shown in Figs. 1(a) and 1(b), respectively. It is shown that the time required for the flow to reach the maximum value of heat release decreases with the increase of turbulent Mach number. Zhao *et al*. [53] suggested that the ignition delay time decreases monotonically with the increase of initial temperature at a given initial pressure. In our simulations, the initial pressure and temperature are identical for three turbulent Mach numbers. However, the higher fluctuating temperature at higher turbulent Mach number leads to smaller ignition delay time. This results in the observation that the time needed to reach the maximum reaction rate is shorter at higher turbulent Mach number. The total normalized heat release $\langle\Theta\rangle(\gamma-1)M^2$ during the entire chemical reaction process at three turbulent Mach numbers is nearly equal to each other, since the area integrals beneath the curves as shown in Fig. 1(a) are nearly identical. Correspondingly, the averaged temperature in Fig. 1(b) starts to increase at $t/\tau > 50$ and approaches the maximum value at $t/\tau > 100$. The averaged temperature for three turbulent Mach numbers is nearly identical at the end of chemical reaction. Figure 1(c) shows the temporal variation of averaged density of OH. It is observed that the time for the maximum radical production is nearly identical to the time for the maximum heat release. The temporal variation of the averaged magnitude of density gradient $\mathbb{G}(\rho)$ is shown in Fig. 1(d), where $\mathbb{G}(\rho) = \sqrt{\langle(\partial\rho/\partial x_1)^2 + (\partial\rho/\partial x_2)^2 + (\partial\rho/\partial x_3)^2\rangle}$. The magnitudes of the density gradient for three turbulent Mach numbers decrease when heat release is strong at $t/\tau > 50$. The values of the density gradient magnitude at the end of the chemical reaction ($t/\tau > 100$) for three turbulent Mach numbers are significantly smaller than their initial values. The observation suggests that heat release suppresses flow compressibility during the chemical reaction

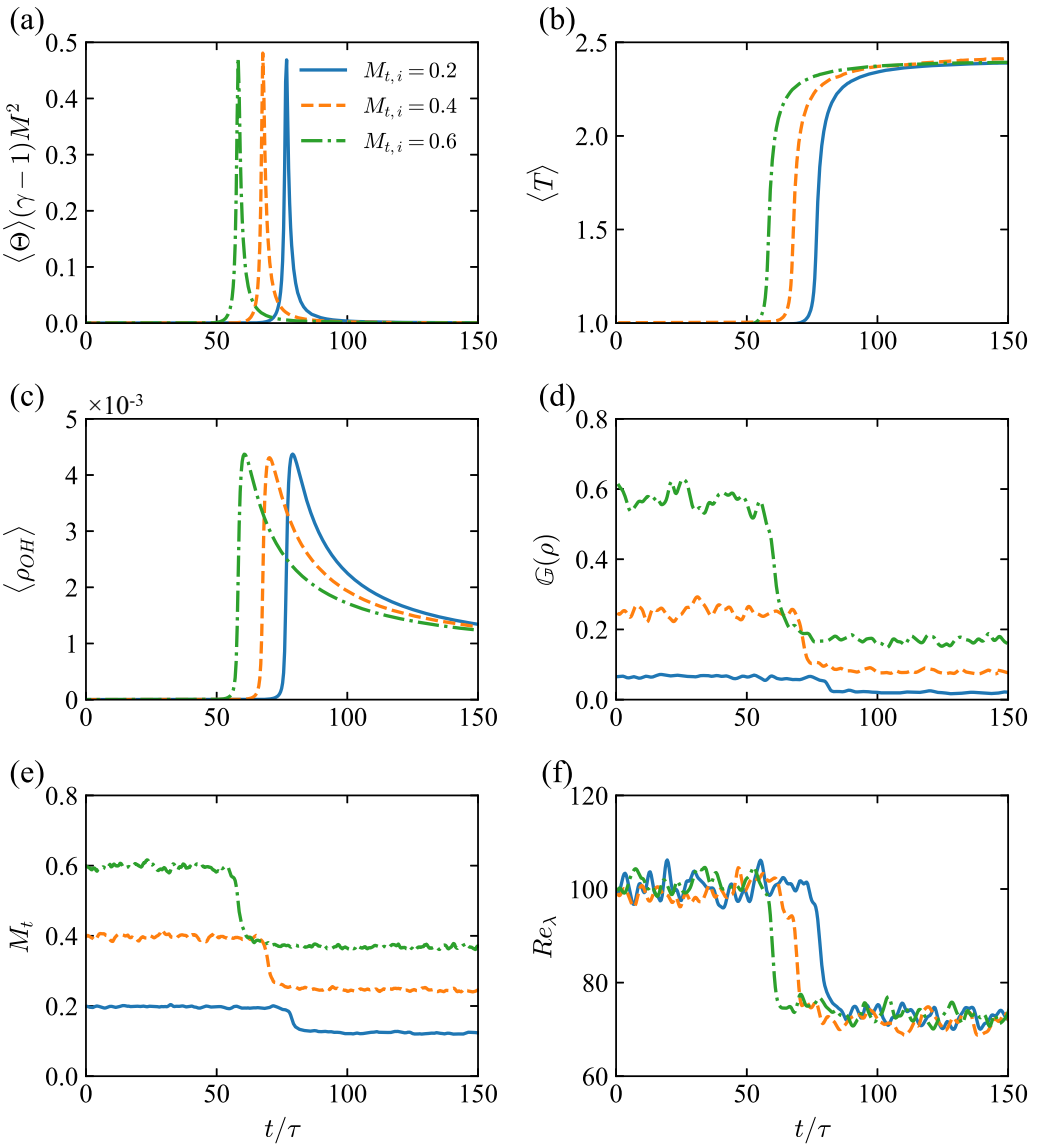

FIG. 1. Temporal variation of flow statistics at $M_{t,i} = 0.2$, 0.4, 0.6: (a) normalized averaged heat release $\langle\Theta\rangle(\gamma-1)M^2$; (b) averaged temperature $\langle T\rangle$; (c) averaged density of species OH $\langle\rho_{\mathrm{OH}}\rangle$; (d) averaged magnitude of density gradient $\mathbb{G}(\rho)$; (e) turbulent Mach number M_t; (f) Taylor Reynolds number Re_λ.

process and the effect is more evident at larger turbulent Mach numbers. The temporal variations of turbulent Mach number M_t and Taylor Reynolds number Re_λ are shown in Figs. 1(e) and 1(f), respectively. It is found that both M_t and Re_λ decrease during the reaction process due to the increase of the averaged temperature.

We employ the method suggested by Malik *et al*. [54] to estimated the nonstretched laminar flame speed s_L at given dimensional temperature, pressure, and equivalence ratio for H_2/air combustion. Figure 2(a) shows the temporal variation of normalized laminar flame speed. The values of initial laminar flame speed $s_{L,init}$ are calculated using initial parameters before the activation of the chemical reaction, and the dimensional values of $s_{L,init}$ are 6.40, 7.94, and 8.35 m/s for initial

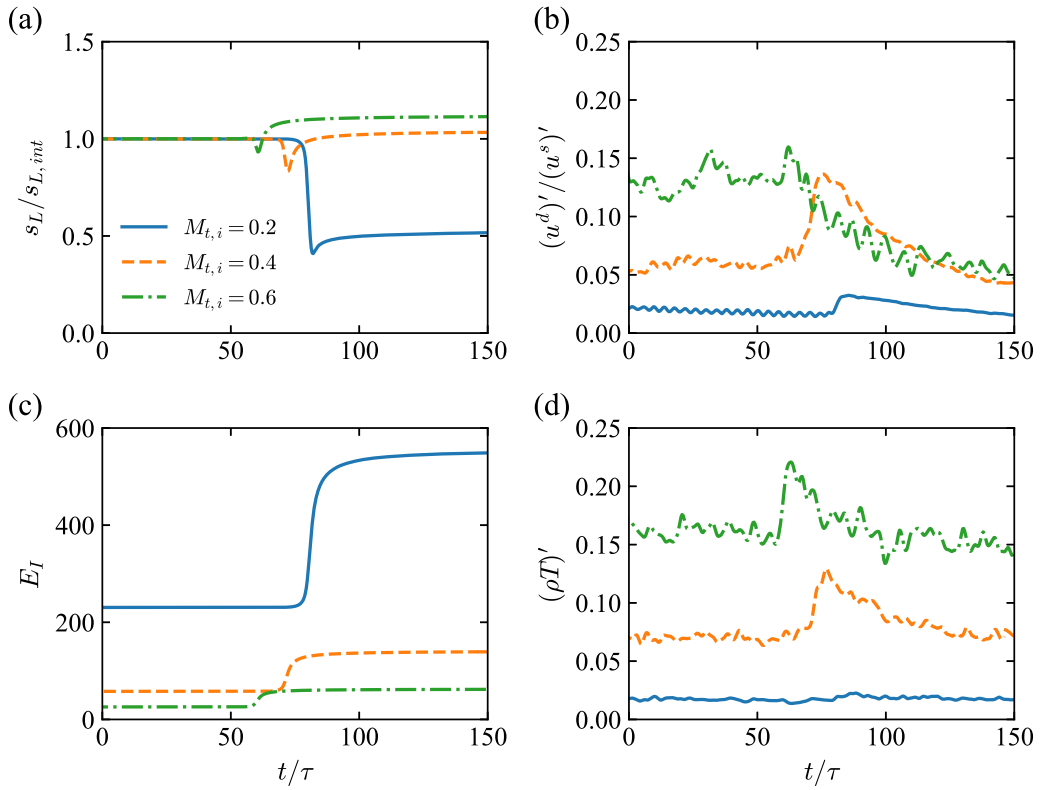

FIG. 2. Temporal variation of flow statistics at $M_{t,i} = 0.2$, 0.4, 0.6: (a) laminar flame speed, s_L; (b) ratio of r.m.s. values of dilatational velocity component to solenoidal velocity component, $(u^d)'/(u^s)'$; (c) internal energy, E_I; (d) r.m.s. value of ρT, $(\rho T)'$.

turbulent Mach numbers 0.2, 0.4, and 0.6, respectively. It is found that the laminar flame speed decreases slightly during the strong heat release period and then increases when heat release is weak at the end of the chemical reaction. The temporal variation of the ratio of r.m.s. values of the dilatational velocity component to that of the solenoidal component is presented in Fig. 2(b). Here the Helmholtz decomposition is applied to decompose the velocity field $\boldsymbol{u}$ into a solenoidal component $\boldsymbol{u}^s$ and a dilatational component $\boldsymbol{u}^d$ [37]: $\boldsymbol{u} = \boldsymbol{u}^s + \boldsymbol{u}^d$, where $\nabla \cdot \boldsymbol{u}^s = 0$ and $\nabla \times \boldsymbol{u}^d = 0$. The r.m.s. values of the two components of velocity are $(u^d)' = \sqrt{\langle (u_1^d)^2 + (u_2^d)^2 + (u_3^d)^2 \rangle}$ and $(u^s)' = \sqrt{\langle (u_1^s)^2 + (u_2^s)^2 + (u_3^s)^2 \rangle}$, respectively. It is observed that the normalized r.m.s. value of the dilatational velocity component increases during the strong heat release period and then decreases when the chemical reaction is weak for three turbulent Mach numbers. The temporal variation of internal energy E_I and r.m.s. value of ρT are shown in Figs. 2(c) and 2(d), respectively. Here $(\rho T)' = \sqrt{\langle (\rho T - \langle \rho T \rangle)^2 \rangle}$ and can be used to assess the fluctuating property of the internal energy. It is shown that the internal energy E_I increases evidently when the reaction heat release is strong at three turbulent Mach numbers. The observation suggests that the released heat of reaction is transferred to internal energy in a short time. Meanwhile, the strong heat release leads to evident fluctuations of ρT, especially for $M_{t,i} = 0.4$ and 0.6.

We plot the temporal variations of averaged kinetic energy and kinetic energy transfer terms in Fig. 3 to evaluate the kinetic energy change during the chemical reaction process. According to Eq. (12) [37–40], we define the total kinetic energy dissipation rate as $\epsilon_T = -\langle p\theta \rangle + \langle \epsilon_V \rangle$. The total kinetic energy dissipation rate represents the total conversion rate of kinetic energy into internal

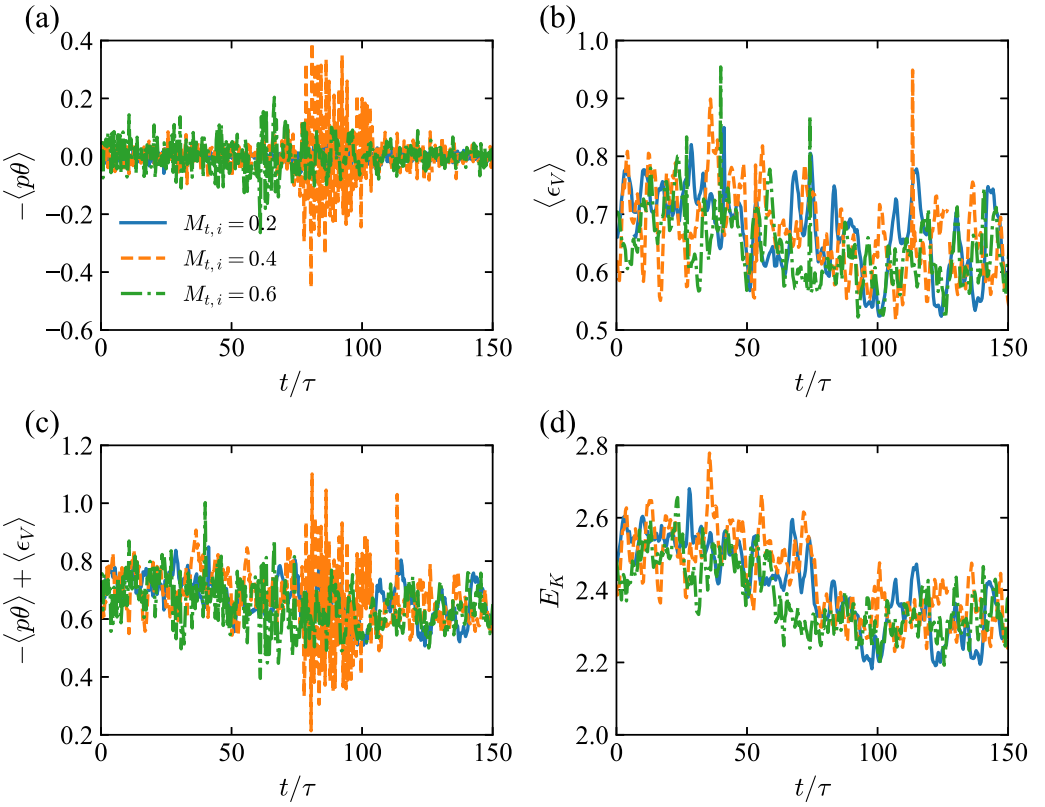

FIG. 3. Temporal variation of flow statistics at $M_{t,i} = 0.2, 0.4, 0.6$: (a) averaged pressure-dilatation $\langle -p\theta \rangle$; (b) averaged viscous dissipation rate $\langle \epsilon_V \rangle$; (c) total kinetic energy dissipation rate $\langle -p\theta \rangle + \langle \epsilon_V \rangle$; (d) averaged kinetic energy E_K.

energy, and $\epsilon_V = (1/\mathrm{Re})\sigma_{ij}(\partial u_i/\partial x_j)$. $\epsilon_{inj} = \mathcal{F}_i u_i$ represents the energy injected by the large-scale forcing [40]. As shown in Figs. 3(a) and 3(b), the averaged pressure dilatation $\langle -p\theta \rangle$ fluctuates evidently in the strong heat release phase at $50 < t/\tau < 100$, while the averaged viscous dissipation rate $\langle \epsilon_V \rangle$ also fluctuates during the entire reaction process. The averaged kinetic energy is defined as $E_K = \langle \mathcal{E}_K \rangle$. As shown in Fig. 3(c), the averaged pressure dilatation has a significant contribution to the total dissipation rate. Due to the effects of heat release, the averaged kinetic energy decreases at $t/\tau > 80$ as shown in Fig. 3(d).

Through the observations of the temporal variations of flow statistics in Figs. 1 to 3, we find that heat release by chemical reaction plays an important role in characterizing flow behaviors during the reaction process. At the initial period after the activation of the chemical reaction, the reaction rate and heat release are weak, and the compressibility of the flow is characterized by the initial turbulent Mach numbers. As chemical reaction proceeds when heat release is strong, the dilatational component of velocity increases due to the fact that energy is transferred from internal energy to the dilatational mode of kinetic energy [35,55]. When internal energy increases due to the reaction heat release, the mean temperature of the mixture raises. Based on the above observations, we roughly divide the entire chemical period into three phases to distinguish different flow features in each period of the reaction process. The three phases are the initial reaction phase ($0 < t/\tau < 50$, subscript i), strong heat release phase ($50 < t/\tau < 100$, subscript s), and reaction end phase ($100 < t/\tau < 150$, subscript e). The subsequent discussions of flow statistics are specified in the different reaction phases.

TABLE I. Temporal average of flow statistics based on flow data of 256^3 grid.

$M_{t,i}$	$\langle T\rangle_i$	$\langle\mu\rangle_i$	$\langle c\rangle_i$	$\langle\epsilon_V\rangle_i$	$-\langle p\theta\rangle_i$	$\langle\mathcal{E}_K\rangle_i$	$(\partial\langle\mathcal{E}_K\rangle/\partial t)_i$	$\langle u'\rangle_i$
0.2	1.00	1.00	21.97	0.71	5×10^{-4}	2.51	-4×10^{-4}	2.26
0.4	1.00	1.00	21.97	0.72	4×10^{-3}	2.53	-8×10^{-5}	2.25
0.6	1.00	1.00	21.97	0.69	8×10^{-3}	2.48	-3×10^{-4}	2.48
$M_{t,i}$	$\langle T\rangle_s$	$\langle\mu\rangle_s$	$\langle c\rangle_s$	$\langle\epsilon_V\rangle_s$	$-\langle p\theta\rangle_s$	$\langle\mathcal{E}_K\rangle_s$	$(\partial\langle\mathcal{E}_K\rangle/\partial t)_s$	$\langle u'\rangle_s$
0.2	1.62	1.43	28.25	0.65	-5×10^{-4}	2.37	-7×10^{-4}	2.19
0.4	1.84	1.56	28.67	0.66	-2×10^{-3}	2.42	-3×10^{-4}	2.18
0.6	2.11	1.71	30.57	0.63	-5×10^{-3}	2.34	-3×10^{-3}	2.16
$M_{t,i}$	$\langle T\rangle_e$	$\langle\mu\rangle_e$	$\langle c\rangle_e$	$\langle\epsilon_V\rangle_e$	$-\langle p\theta\rangle_e$	$\langle\mathcal{E}_K\rangle_e$	$(\partial\langle\mathcal{E}_K\rangle/\partial t)_e$	$\langle u'\rangle_e$
0.2	2.38	1.85	32.68	0.63	8×10^{-5}	2.30	-6×10^{-4}	2.16
0.4	2.38	1.85	32.68	0.62	3×10^{-3}	2.31	-2×10^{-3}	2.15
0.6	2.38	1.85	32.68	0.62	2×10^{-3}	2.33	-1×10^{-3}	2.15

In Fig. 3(d) we find that the averaged kinetic energy decreases after strong heat release. Now we show the temporal average of flow statistics over different reaction phases in Table I to further explain the decrease of averaged kinetic energy as well as flow compressibility after the strong heat release during the chemical reaction process. It is observed that the averaged temperatures increase from 1.0 to 2.38 for three turbulent Mach numbers after strong heat release. Consequently, the averaged viscosity coefficients increase from 1.0 to 1.85. The sound velocity is defined as $c=\sqrt{\gamma\mathbb{R}_{\rm mix}T}$, and $\mathbb{R}_{\rm mix}$ is the gas constant of the mixture. It is shown that the sound velocities for three turbulent Mach numbers also increase due to the increase of temperature. According to Eq. (12), the averaged viscous dissipation rate of kinetic energy not only depends on viscosity coefficient but also is closely related to velocity gradients. It is shown that the averaged viscous dissipation rates of kinetic energy decrease from approximately 0.7 to 0.6 after the strong heat release period for three turbulent Mach numbers. The pressure-dilatation correlation plays an important role in energy transfer for compressible turbulence [40]. We can find that $-\langle p\theta\rangle$ are all negative for three turbulent Mach numbers during the strong heat release phase. According to the definition of the total kinetic energy dissipation rate $\epsilon_T=-\langle p\theta\rangle+\langle\epsilon_V\rangle$, we can find that the energy transfer rate from kinetic energy to internal energy decreases; however, we cannot determine the variations of the averaged kinetic energy considering only the change of total the kinetic energy dissipation rate as indicated by Eq. (12). The averaged value of external forcing also plays an important role in deciding the temporal variation of averaged kinetic energy. To further evaluate the variation rate of averaged kinetic energy, the time derivatives of the averaged kinetic energy for three reactions phases are calculated. It is shown that the time derivatives of averaged kinetic energy are negative throughout the entire chemical reaction process. Consequently, the averaged kinetic energy as well as the r.m.s values of the velocity decrease. Additionally, we show the temporally averaged velocity spectra for three turbulent Mach numbers in Fig. 4 to explain the decrease of averaged kinetic energy. The spectra for each turbulent Mach number are averaged values in three reaction phases. With the increase of temperature after strong heat release, the viscosity coefficient increases. The increased viscosity coefficient leads to the decrease of the Taylor Reynolds number. Under this situation, the flow becomes smoother and the spectra of the velocity become shorter as shown in Fig. 4. Meanwhile, due to the decrease of the Taylor Reynolds number, the kinetic energy cascade becomes weaker, and thus the external energy injection is reduced. When the new equilibrium is established, the averaged kinetic energy decreases. It is noted that after strong heat release, the turbulent Mach number decreases. The combined effects of the increased sound velocity and the decreased velocity fluctuations lead to the overall decrease of flow compressibility after strong heat release. The temporal averaged values of sound velocity and the r.m.s. values of velocity as shown in Table I suggest that the increased sound velocity is the major reason for the decrease of flow compressibility.

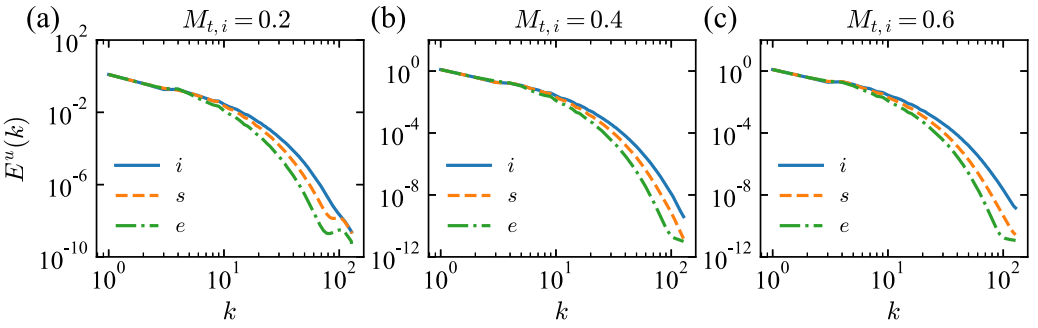

FIG. 4. Temporally averaged velocity spectra for three reaction phases at $M_t = 0.2$, 0.4, and 0.6.

To further reveal the effects of chemical reaction process and heat release on flow compressibility, Fig. 5 shows the instantaneous isosurfaces of normalized velocity divergence θ/θ' for three turbulent Mach numbers 0.2, 0.4, and 0.6 and at various normalized reaction time. The three selected

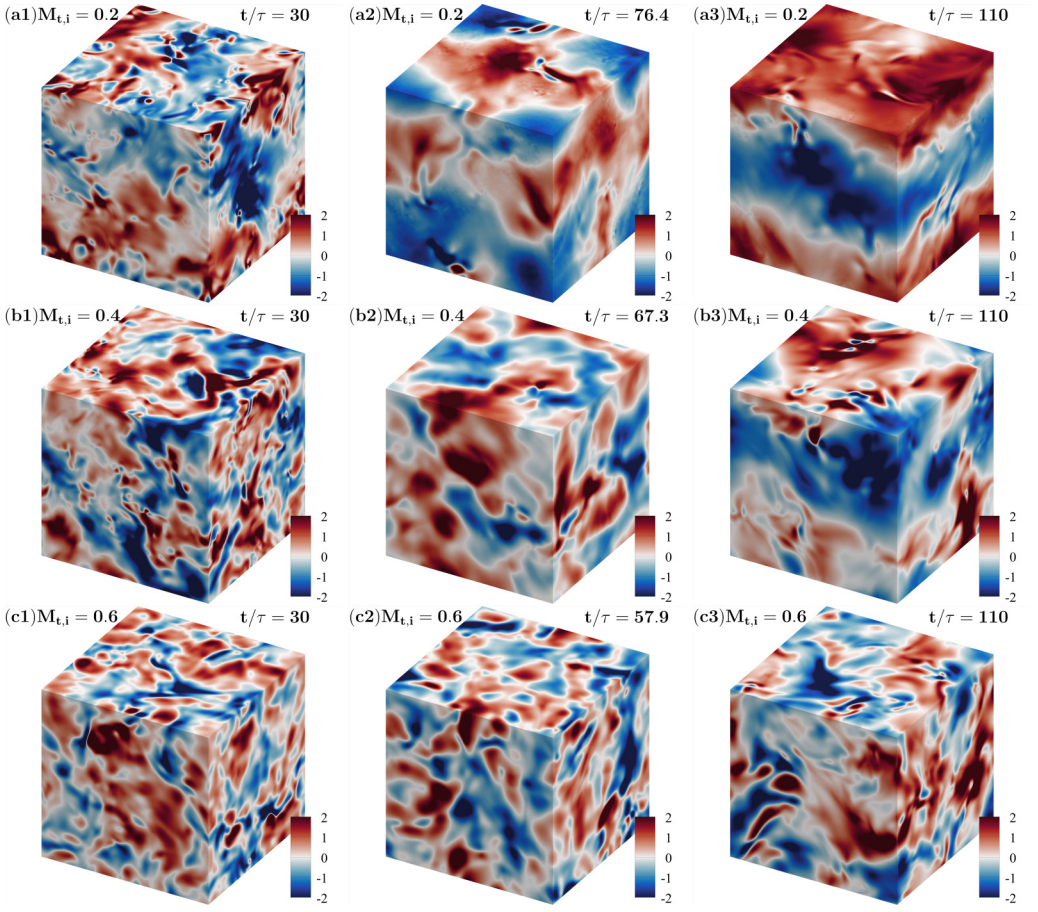

FIG. 5. Instantaneous isosurfaces of normalized velocity divergence θ/θ' for the simulations with 256^3 grid resolution at $M_{t,i} = 0.2$, 0.4, 0.6 and at various normalized reaction times: (a1)–(a3) $M_{t,i} = 0.2$; (b1)–(b3) $M_{t,i} = 0.4$; (c1)–(c3) $M_{t,i} = 0.6$.

TABLE II. Specification of DNS parameters and resulting flow statistics.

Resolution	$\mathrm{Re}_{\lambda,i}$	$\mathrm{Re}_{\lambda,e}$	$M_{t,i}$	$M_{t,e}$	$(\eta/\Delta x)_i$	$(\eta/\Delta x)_e$	$(L_I/\eta)_i$	$(L_I/\eta)_e$	Ka_i	Ka_e
64^3	34	21	0.17	0.11	1.02	1.52	18.7	13.2	55	416
64^3	34	21	0.34	0.21	1.03	1.52	18.8	13.2	35	54
64^3	34	21	0.51	0.32	1.03	1.53	18.8	13.1	32	42
128^3	62	42	0.18	0.11	1.05	1.66	33.3	22.4	209	1135
128^3	62	42	0.36	0.22	1.05	1.66	33.3	22.5	135	176
128^3	63	43	0.54	0.34	1.07	1.67	33.1	22.5	119	147
256^3	99	72	0.20	0.12	0.98	1.60	62.5	40.5	960	4564
256^3	100	73	0.40	0.25	0.99	1.61	62.2	41.1	610	736
256^3	101	73	0.60	0.37	0.99	1.64	61.8	41.0	547	568

normalized reaction times for each turbulent Mach number correspond to chemical reaction instants in the initial period when heat release is weak ($t/\tau = 30$), at the peak heat release moment ($t/\tau = 76.4$ for $M_{t,i} = 0.2$; $t/\tau = 67.3$ for $M_{t,i} = 0.4$; $t/\tau = 57.9$ for $M_{t,i} = 0.6$), and in the reaction end period ($t/\tau = 110$) when heat release is weak. It is observed that at t/τ=30 as shown in Figs. 5(a1)–5(c1) which corresponds to the instants during the initial reaction period in Fig. 1(a), the length scales of compression and expansion flow structures are small. With the increase of initial turbulent Mach number, for example, at $M_{t,i} = 0.6$, more blue streaky structures are which associated with strong compression regions are observed. At the maximum heat release time as shown in Figs. 5(a2)–5(c2) for each turbulent Mach number, the length scales of compression and expansion structures become larger compared to those at the initial period. When the chemical reaction approaches the end of the chemical reaction at t/τ=110 as shown in Figs. 5(a3)–5(c3), large patches of compression and expansion regions are sparsely distributed in the flow field, implying that the length scales of compression and expansion structures become relatively large and the flow compressibility becomes smaller.

The specification of simulated parameters and resulting flow statistics at the initial reaction phase and reaction end phase are listed in Table II. We present flow statistics averaged in those two reaction phases to evaluate the flow state change resulting from the chemical reaction. The Taylor Reynolds number and turbulent Mach number decrease after strong heat release at three initial turbulent Mach numbers. The decrease of the two statistics is closely related to the increase of the averaged temperature as shown in Fig. 1(b) and the decrease of velocity fluctuations shown in Fig. 2(b). The Kolmogorov length scale is defined by $\eta = [\langle \mu/(\mathrm{Re}\,\rho)\rangle^3/\epsilon]^{1/4}$ [16,37], where the dissipation rate of the kinetic energy per unit mass is given by $\epsilon = \langle \sigma_{ij} S_{ij}/(\mathrm{Re}\,\rho)\rangle$. The magnitude of Kolmogorov length scale η represents the dissipation-range resolution, which plays a significant role in the grid convergence of velocity statistics in DNS [56]. As shown in Table II, the resolution parameter $\eta/\Delta x$ lies within the range between 0.98 and 1.07 at the initial reaction phase, where Δx denotes the grid length in each direction. It is straightforward to derive that $3.08 < k_{\max}\eta < 3.36$, where the largest wave number $k_{\max}$ is half of the number of grids N in each direction: $k_{\max} = N/2 = \pi/\Delta x$. At the end phase of chemical reaction, the resolution parameter $\eta/\Delta x \geqslant 1.52$, which suggests that reaction heat release leads to an increase of the Kolmogorov length scale. Previous DNS results [57] showed that the resolution parameter $\eta/\Delta x \geqslant 0.7$ is good enough for convergence of high-order moments of velocity gradients. Therefore, the overall statistics are well converged in current numerical simulations [30,47]. The ratio of L_I/η lies within the range $18.7 \leqslant L_I/\eta \leqslant 62.5$ at the initial reaction phase and decreases at the reaction end phase. The Karlovitz number is used to classify various combustion regimes of turbulence/flame interaction and is defined as the ratio of the flame timescale τ_F to the Kolmogorov timescale τ_η [58]. Alternatively, the Karlovitz number can also be calculated by the ratio of the flame length scale $\mathcal{L}_F$ to the Kolmogorov length scale η [59]: $\mathrm{Ka} = \mathcal{L}_F^2/\eta^2$, where $\mathcal{L}_F = \nu/(Sc\ s_L)$ and s_L denotes the nonstretched laminar flame speed.

TABLE III. Flow statistics in reaction initial phase and strong heat release phase.

Resolution	$M_{t,i}$	$S_{3,i}$	$S_{3,s}$	θ'_i	θ'_s	ω'_i	ω'_s	$(\theta'/\omega')_i$	$(\theta'/\omega')_s$	$(S'/\omega')_i$	$(S'/\omega')_s$
64^3	0.17	−0.31	−0.30	0.02	0.01	3.86	3.35	0.006	0.003	0.707	0.707
64^3	0.34	−0.33	−0.28	0.08	0.03	3.81	3.24	0.021	0.009	0.707	0.707
64^3	0.51	−0.33	−0.21	0.24	0.14	3.85	3.22	0.061	0.043	0.710	0.709
128^3	0.18	−0.43	−0.40	0.04	0.02	5.89	4.61	0.006	0.003	0.707	0.707
128^3	0.36	−0.39	−0.40	0.15	0.22	5.86	4.86	0.025	0.045	0.708	0.709
128^3	0.54	−0.37	−0.38	0.62	0.50	5.67	5.65	0.108	0.088	0.713	0.716
256^3	0.20	−0.47	−0.42	0.08	0.08	10.77	7.64	0.008	0.011	0.707	0.707
256^3	0.40	−0.46	−0.43	0.32	0.47	10.62	7.68	0.031	0.058	0.707	0.709
256^3	0.60	−0.45	−0.42	1.20	0.68	10.36	7.59	0.116	0.089	0.717	0.713

For the low Taylor Reynolds number cases at 64^3 grid resolution, the initial Karlovitz numbers are less than 100, which suggests that the flame locates in the thin reaction zone. The initial Karlovitz numbers in the cases of 128^3 and 256^3 grid resolutions are larger than 100, which indicates that the initial flame locates in the broken reaction zone. The laminar flame speed s_L changes dramatically at the reaction end phase, especially at $M_{t,i} = 0.2$ as shown in Fig. 2(a). The Karlovitz numbers at the reaction end phase are larger than their initial values for three initial turbulent Mach numbers.

Table III shows the resulting flow statistics based on simulated data in the reaction initial phase and the strong heat release phase. The velocity derivative skewness S_3 is calculated by

$$S_3 = \frac{[\langle(\partial u_1/\partial x_1)^3 + (\partial u_2/\partial x_2)^3 + (\partial u_3/\partial x_3)^3\rangle]/3}{[\langle(\partial u_1/\partial x_1)^2 + (\partial u_2/\partial x_2)^2 + (\partial u_3/\partial x_3)^2\rangle/3]^{3/2}}. \tag{23}$$

As shown in the table, the magnitudes of S_3 decrease slightly with the increase of turbulent Mach number for the situations of 128^3 and 256^3 grid resolutions at the initial reaction phase. The strong heat release leads to a slight decrease of the magnitudes of S_3 at three turbulent Mach numbers after strong heat release. The r.m.s. value of velocity divergence is calculated by $\theta' = \sqrt{\langle\theta^2\rangle}$. It is found that θ' is enhanced at $M_{t,i} = 0.4$ for the situations of 128^3 and 256^3 grid resolutions during the strong heat release phase compared to those at the initial reaction phase. For results at $M_{t,i} = 0.6$, the strong heat release leads to rapid transfer of kinetic energy into internal energy, and thus results in the decrease of θ' during the strong heat release phase. Vorticity is defined by $\omega = \nabla \times \boldsymbol{u}$. The r.m.s. value of vorticity magnitude is obtained by $\omega' = \sqrt{\langle\omega_1^2 + \omega_2^2 + \omega_3^2\rangle}$. It is shown that ω' is insensitive to the change of turbulent Mach number in our numerical simulations at both the initial reaction phase and the intense heat release phase. However, ω' decreases during the strong heat release phase compared to the initial reaction phase. The r.m.s. value of the strain rate tensor is defined by $S' = \sqrt{\langle S_{ij}S_{ij}\rangle}$. It is shown that S'/ω' is insensitive to the change of turbulent Mach number and reaction heat release. The statistics of temporally averaged flow quantities conditioned on a specified time period, for example, on the strong heat release phase, is more meaningful to show the influence of reaction heat release on turbulence than the temporal average conditioned on the entire reaction process.

The above analyses suggest that the quantities of flow statistics exhibit dependence on the duration of each reaction phase and the amount of heat release during the chemical reaction process. To exclude the influence of initial conditions and to obtain a general applicability of current qualitative results considering the effects of heat release, we provide additional simulations using a 64^3 grid to assess the influence of initial conditions on flow statistics in Appendix B. As shown in Figs. 22 through 25, we find that even through the quantities of heat release rate, reaction rate, and the extent for the decrease of turbulent Mach number as well as the Taylor Reynolds number are different for different initial conditions, the variations of the flow statistics after reaction heat

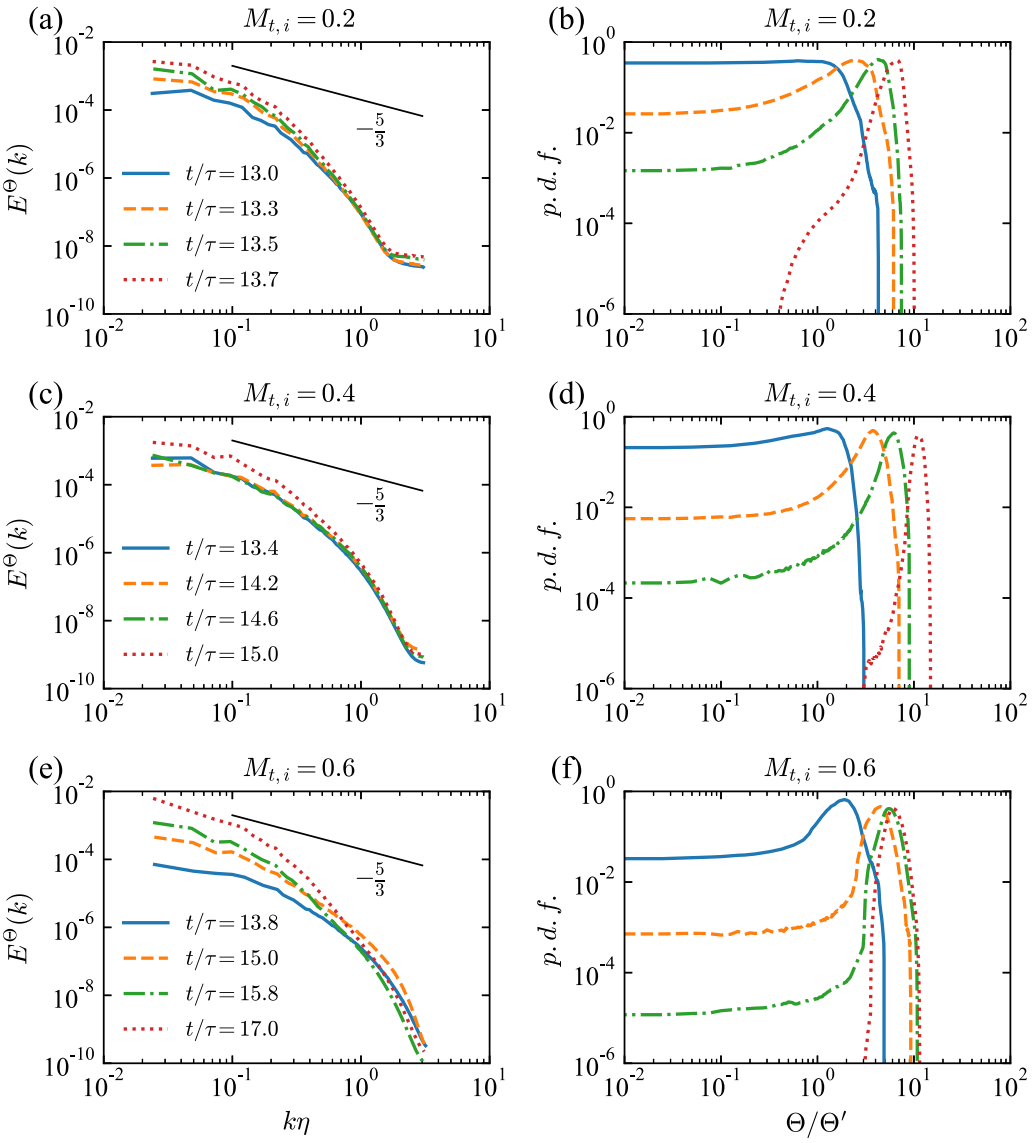

FIG. 6. Spectrum of heat release Θ and PDF of normalized heat release Θ/Θ' at various normalized reaction time: (a), (c), (e) spectra of Θ at $M_{t,i} = 0.2$, 0.4, 0.6; (b), (d), (f) PDF of Θ/Θ' at $M_{t,i} = 0.2$, 0.4, 0.6.

release are similar. The temporal averaged flow quantities in different reaction phases as shown in Tables IX and X are also similar to each other.

We plot the the spectrum of heat release $E^{\Theta}(k)$ and the probability density function (PDF) of normalized reaction heat release Θ/Θ' at $M_{t,i} = 0.2$, 0.4, and 0.6 for different normalized reaction time t/τ in Fig. 6, where $\int_0^{\infty} E^{\Theta}(k)\,dk = \langle(\Theta - \Theta_0)^2\rangle$ and Θ_0 is the mean value of heat release. The normalized reaction time $13 < t/\tau < 17$ corresponds to the time period in the initial reaction phase. It is observed from the left column of Fig. 6 that with the increase of normalized reaction time, $E^{\Theta}(k)$ at small $k\eta$ ($k\eta < 0.1$) increases due to the increase of heat release. $E^{\Theta}(k)$ at large $k\eta$ ($k\eta > 1$) is nearly unaffected during this period. The observation suggests that the spectrum of heat

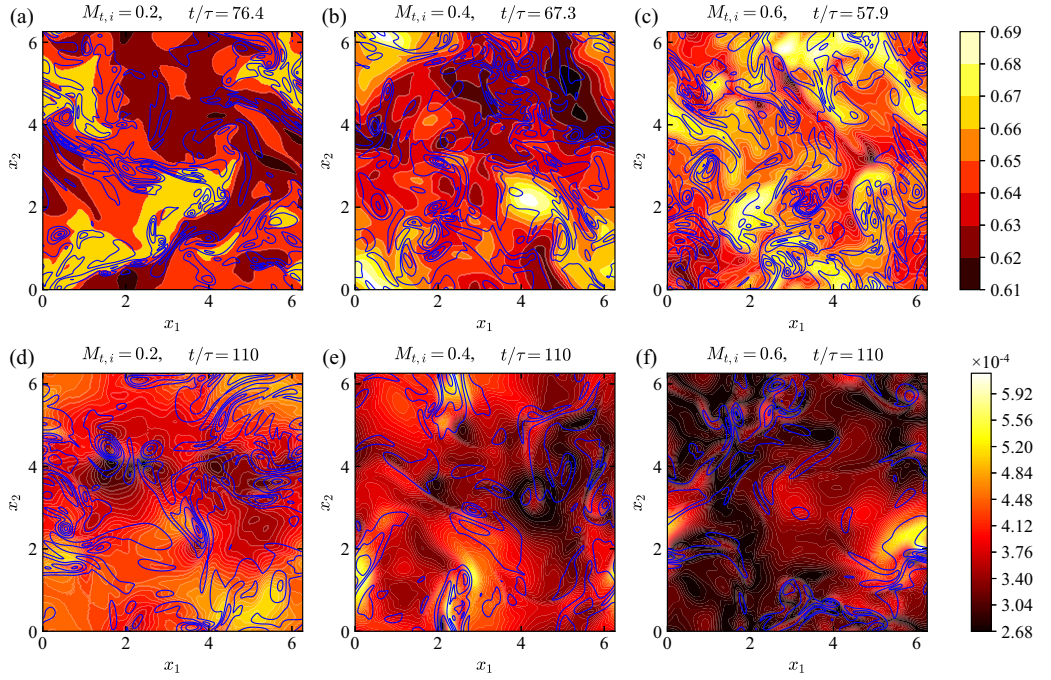

FIG. 7. Instantaneous contours of normalized heat release Θ/Θ' and isolines of normalized magnitude of vorticity ω/ω' (blue lines) at various normalized reaction time at $M_{t,i} = 0.2$, 0.4, 0.6: (a), (d) $M_{t,i} = 0.2$, (b), (e) $M_{t,i} = 0.4$, (c), (f) $M_{t,i} = 0.6$.

release is more likely to be enhanced at large scales at the initial phase of chemical reaction. It can also be found that the spectrum of heat release does not exhibit the $-5/3$ law in the inertial range. The right column of Fig. 6 shows the PDFs of Θ/Θ'. The normalized reaction time t/τ corresponds to the time shown in the left column for each turbulent Mach number. It is observed that the left tails of the PDFs are evidently longer than their right tails. With the increase of normalized reaction time, the left tails becomes shorter and the overall PDFs shift towards the right corresponding to the increase of heat release.

To further reveal the temporal variations of heat release and vortical structures, we depict the instantaneous contours of normalized heat release Θ/Θ' superimposed by isolines of normalized magnitude of vorticity ω/ω' at the normalized reaction time of maximum heat release for each turbulent Mach number and at t/τ=110 in the reaction end phase in Fig. 7. It can be observed that the structures of strong heat release can be found in both small and large structures. The strong heat release structures at the two normalized reaction times are scattered in the flow field and belong to the broken reaction zone according to the combustion regime classification for the Karlvoitz number Ka $>$ 100 at three turbulent Mach numbers. At the maximum heat release time for three turbulent Mach numbers as shown in Figs. 7(a)–7(c), the vortical structures are not directly associated with the heat release structures. At t/τ=110 in the reaction end phase, the vortical structures are more likely to be found in the weak heat release regions as shown in Figs. 7(d)–7(f).

We depict the average of normalized magnitude of vorticity, strain rate tensors, enstrophy production, and its dilatational component conditioned on the normalized velocity divergence θ/θ' at $M_{t,i} = 0.2$, 0.4, 0.6 in Fig. 8. The temporal average is based on simulated data in the strong heat release phase ($50 < t/\tau < 100$). As shown in Fig. 8(a), the conditional average of ω/ω' increases with the increase of the velocity divergence magnitude in strong compression and expansion regions. In compression regions, the conditional averages of ω/ω' for three turbulent Mach numbers are

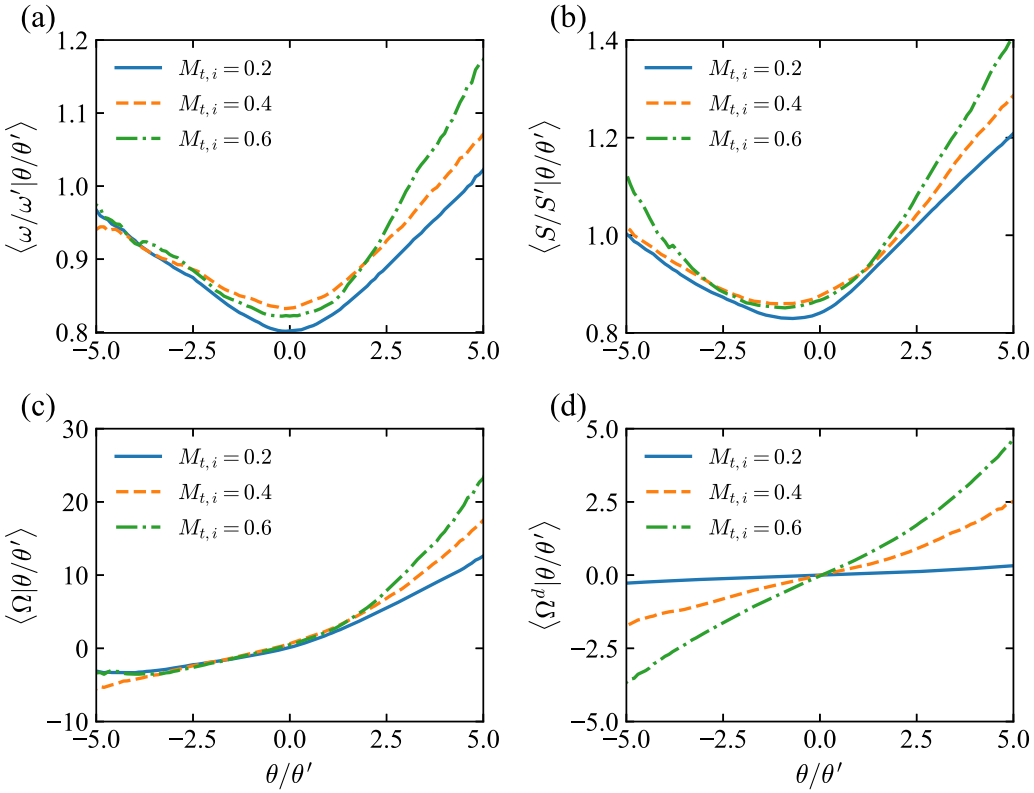

FIG. 8. Conditional average of the normalized magnitude of vorticity, strain rate tensors, enstrophy production, and its dilatational component at $M_{t,i} = 0.2, 0.4, 0.6$: (a) $\langle \omega/\omega' | \theta/\theta' \rangle$; (b) $\langle S/S' | \theta/\theta' \rangle$; (c) $\langle \Omega | \theta/\theta' \rangle$; (d) $\langle \Omega^d | \theta/\theta' \rangle$.

close to each other. The conditional average of ω/ω' increases with the increase of initial turbulent Mach number in the expansion regions. In Fig. 8(b) we observe that the conditional average of S/S' increases linearly with the increase of velocity divergence magnitude in strong compression regions and strong expansion regions. Moreover, the conditional average of S/S' in strong compression regions and strong expansion regions increases with the increase of initial turbulent Mach number. We further consider the enstrophy production $\omega_i\omega_j S_{ij}$ by the strain rate tensor S_{ij} via the vortex stretching and tilting mechanism. We denote the normalized enstrophy production and its dilatational component as $\Omega = \omega_i\omega_j S_{ij}/\langle \omega_i\omega_j S_{ij} \rangle$, $\Omega^d = \omega_i\omega_j S^d_{ij}/\langle \omega_i\omega_j S_{ij} \rangle$, respectively. In weakly compressible turbulence [8,60,61], the predominance of vortex stretching over vortex compression causes self-amplification of local vorticity, leading to the fact that the spatial average of enstrophy production is positive, i.e., $\langle \omega_i\omega_j S_{ij} \rangle > 0$. It is found that $\langle \omega_i\omega_j S_{ij} \rangle > 0$ in our numerical simulations of chemically reacting compressible isotropic turbulence at three turbulent Mach numbers. Figures 8(c) and 8(d) show the average of enstrophy production and its dilatational component conditioned on normalized velocity divergence at $M_{t,i} = 0.2, 0.4, 0.6$. It is observed that the conditional average of Ω and Ω^d is negative in strong compression regions, indicating that the interaction between the vorticity and strain rate tensor causes the destruction of enstrophy in strong compression regions. The conditional average of Ω and Ω^d increases rapidly with the increase of normalized velocity divergence in strong expansion regions, suggesting that strong expansion motions significantly enhance the generation of enstrophy and its dilatational component by the interaction between the vorticity and strain rate tensor.

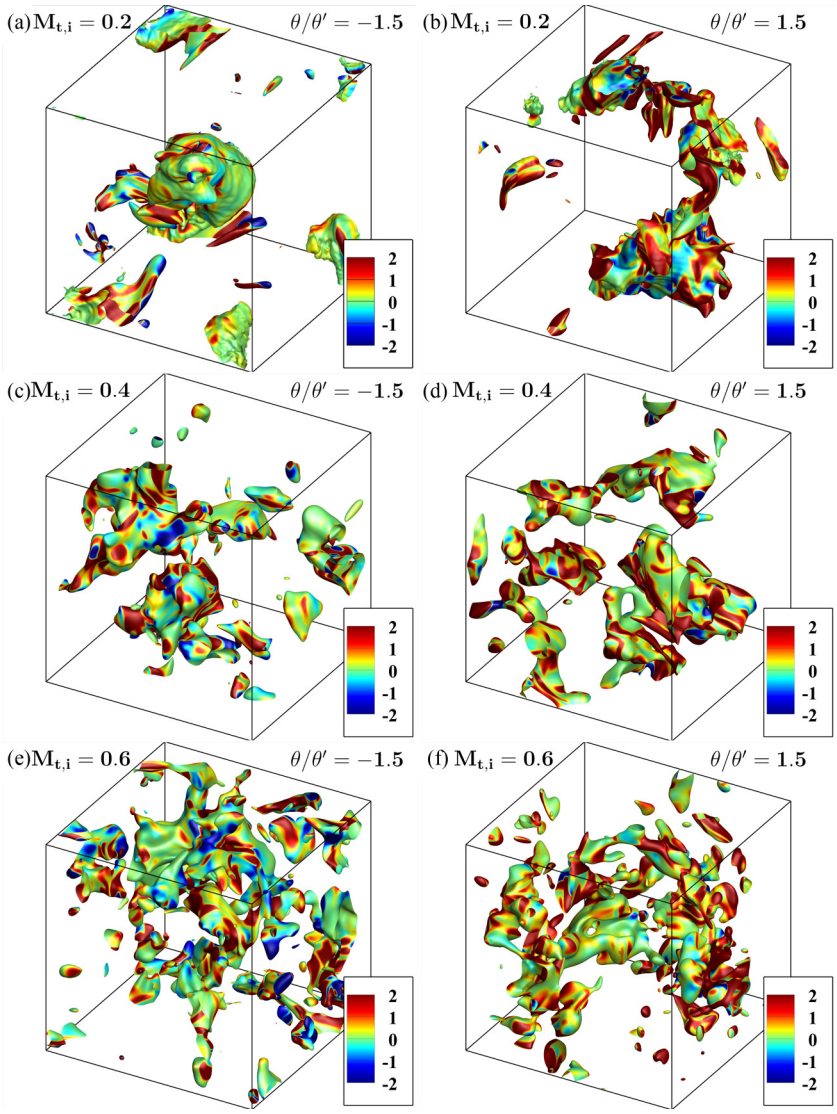

FIG. 9. Isosurfaces of normalized velocity divergence θ/θ' for the simulations with 256^3 grid resolution at the maximum heat release time for each turbulent Mach number at $M_{t,i} = 0.2$, 0.4, 0.6. The isosurfaces are colored by $\omega_i\omega_j S_{ij}/\langle\omega_i\omega_j S_{ij}\rangle$: (a) $\theta = -1.5\theta'$ at $M_{t,i} = 0.2$; (b) $\theta = 1.5\theta'$ at $M_{t,i} = 0.2$; (c) $\theta = -1.5\theta'$ at $M_{t,i} = 0.4$; (d) $\theta = 1.5\theta'$ at $M_{t,i} = 0.4$; (e) $\theta = -1.5\theta'$ at $M_{t,i} = 0.6$; (f) $\theta = 1.5\theta'$ at $M_{t,i} = 0.6$.

We further explore the relation between compression and expansion structures with enstrophy production. Figure 9 displays isosurfaces of velocity divergence of $\theta = -1.5\theta'$ and $\theta = 1.5\theta'$ for $M_{t,i} = 0.2$, 0.4, 0.6 at the maximum heat release time ($t/\tau = 76.4$ at $M_{t,i} = 0.2$; $t/\tau = 67.3$ at $M_{t,i} = 0.4$; $t/\tau = 57.9$ at $M_{t,i} = 0.6$) for each turbulent Mach number. The isosurfaces are cikired by the normalized enstrophy production $\omega_i\omega_j S_{ij}/\langle\omega_i\omega_j S_{ij}\rangle$. It is shown that the number of isosurfaces of $\theta = -1.5\theta'$ and $\theta = 1.5\theta'$ increase with the increase of initial turbulent Mach number. The isosurfaces are bloblike and tubelike in our numerical simulations. Both the positive and negative values of entrophy production $\omega_i\omega_j S_{ij}$ are found on the isosurfaces of $\theta = -1.5\theta'$, and the entrophy production is likely to be positive on the isosurfaces of $\theta = 1.5\theta'$. These observations

are consistent with the previous results on the conditional average of entrophy production $\omega_i\omega_j S_{ij}$ as shown in Fig. 8(c), demonstrating that the interaction between the vorticity and strain rate tensor causes the production of enstrophy in strong expansion regions.

IV. LOCAL FLOW TOPOLOGIES OF COMPRESSIBLE REACTIVE TURBULENCE

1. Topological classification of compressible turbulence

According to the topological classification by Chong *et al*. [1], the local flow pattern at a point in a compressible flow field can be deduced by three invariants of the velocity gradient tensor $A_{ij} = \partial u_i/\partial x_j$. The first, second, and third invariants of A_{ij} are denoted by P, Q, and R, respectively, which are defined by

$$P = -(\xi_1 + \xi_2 + \xi_3) = -\theta, \tag{24}$$

$$Q = \xi_1\xi_2 + \xi_2\xi_3 + \xi_3\xi_1 = \tfrac{1}{2}(P^2 - S_{ij}S_{ij} + W_{ij}W_{ij}), \tag{25}$$

$$R = -\xi_1\xi_2\xi_3 = \tfrac{1}{3}(-P^3 + 3PQ - S_{ij}S_{jk}S_{ki} - 3W_{ij}W_{jk}S_{ki}). \tag{26}$$

Here $S_{ij} = (A_{ij} + A_{ji})/2$ is the strain rate tensor, and $W_{ij} = (A_{ij} - A_{ji})/2$ is rotation rate tensors. It is noted that the first invariant P characterizes the flow dilatation, and the second invariant Q measures the relative importance of enstrophy and strain. Positive values of Q represent that enstrophy dominates over strain, and vice versa [62]. The character of the third invariant R depends on Q, i.e., $Q > 0$, $R < 0$ represents vortex stretching, and $Q > 0$, $R > 0$ represents vortex compression. For $Q < 0$, R is dominated by the strain self-amplification [62]. Three eigenvalues of the velocity gradient tensor are denoted by ξ_i ($i = 1, 2, 3$), which satisfy the following characteristic equation:

$$\xi_i^3 + P\xi_i^2 + Q\xi_i + R = 0. \tag{27}$$

The three invariants can be further decomposed into two parts: a symmetric part and an antisymmetric part:

$$P_s = P = -\theta, \quad Q_s = \tfrac{1}{2}\big(P_s^2 - S_{ij}S_{ji}\big), \quad R_s = \tfrac{1}{3}\big(-P_s^3 + 3P_sQ_s - S_{ij}S_{jk}S_{ki}\big), \tag{28}$$

$$P_w = 0, \quad Q_w = -\tfrac{1}{2}W_{ij}W_{ji}, \quad R_w = 0, \tag{29}$$

where P_s is identical with P. Q_s is the second invariants of the strain rate tensor (i.e., symmetric part of $\partial u_i/\partial x_j$) and Q_w is the second invariants of the rotation rate tensor (i.e., antisymmetric part of $\partial u_i/\partial x_j$). The correlation between Q_s and Q_w can be used to measure the relative importance of flow motions between pure straining motion and pure solid-body rotation. R_s is associated with the strain production [62–64].

The discriminant Δ of the velocity gradient tensor is defined by

$$\Delta = 27R^2 + (4P^3 - 18PQ)R + (4Q^3 - P^2Q^2) \tag{30}$$

If $\Delta < 0$, the three eigenvalues of A_{ij} are all real: $\xi_1 \leqslant \xi_2 \leqslant \xi_3$. On the other hand, if $\Delta > 0$, only one eigenvalue is real, and the two other eigenvalues are complex conjugate pairs, $\xi_{1,2} = \xi_r \pm i\xi_i$ and ξ_3 is real, where ξ_r and ξ_i are real numbers. $\Delta < 0$ and $\Delta > 0$ correspond to the nonfocal regions and focal regions, respectively [1]. The surface $\Delta = 0$ can be split into two surfaces $r^{(1a)}$ and $r^{(1b)}$, given by

$$P(9Q - 2P^2) - 2(-3Q + P^2)^{3/2} - 27R = 0, \tag{31}$$

$$P(9Q - 2P^2) + 2(-3Q + P^2)^{3/2} - 27R = 0. \tag{32}$$

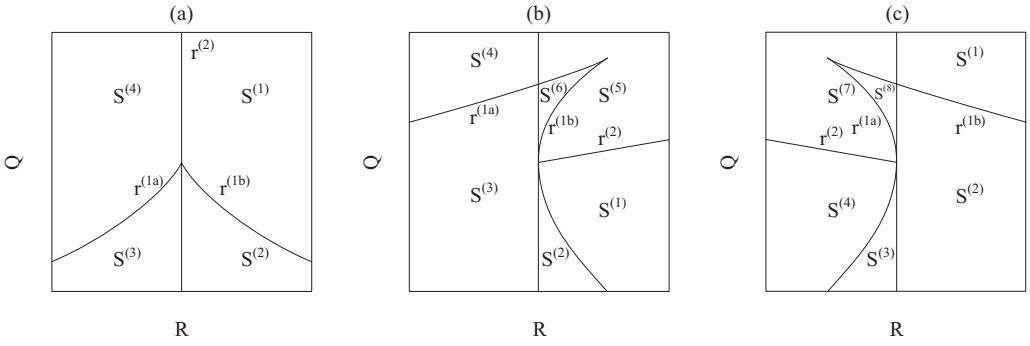

FIG. 10. The topological classifications of three representative Q-R planes: (a) $P = 0$, (b) $P > 0$, and (c) $P < 0$. The description of acronyms for various flow topologies are provided in Table IV.

The two surfaces $r^{(1a)}$ and $r^{(1b)}$ osculate each other to form a cusp. In the region $\Delta > 0$, there is another surface $r^{(2)}$ which contains the points associated with purely imaginary eigenvalues:

$$PQ - R = 0 \tag{33}$$

The P-Q-R space can be partitioned into different spatial regions by the surfaces $r^{(1a)}$, $r^{(1b)}$, $r^{(2)}$ and $R = 0$. $r^{(1a)} = P(Q - 2P^2/9)/3 - 2(-3Q + P^2)^{3/2}/27$ and $r^{(1b)} = P(Q - 2P^2/9)/3 + 2(-3Q + P^2)^{3/2}/27$.

The flow topology can be studied conveniently in the Q-R plane for a given value of P or θ [24,65]. The surfaces $r^{(1a)}$, $r^{(1b)}$, $r^{(2)}$ and $R = 0$ appear simply as curves on the Q-R plane, dividing the plane into different regions corresponding to different topologies. The topological classifications of three representative Q-R planes are plotted in Fig. 10: $P = 0$, $P > 0$, and $P < 0$. The description of acronyms for various flow topologies is given in Table IV. On the plane $P = 0$ as shown in Fig. 10(a), the curves $r^{(1a)}$ and $r^{(1b)}$ are symmetric to each other with respect to the Q axis, and the curve $r^{(2)}$ is coincident with the Q axis. Four different topologies can be identified: UFC, UN/S/S, SN/S/S, and SFS, which are denoted by $S^{(1)}$, $S^{(2)}$, $S^{(3)}$, and $S^{(4)}$, respectively. UN/S/S and SN/S/S are nonfocal structures associated with $\Delta < 0$, while UFC and SFS are focal structures associated with $\Delta > 0$. Specifically, the properties of three eigenvalues of velocity gradient tensor in these topologies are $\xi_1 < 0$, $\xi_2 > 0$, and $\xi_3 > 0$ for UN/S/S; $\xi_1 < 0$, $\xi_2 < 0$, and $\xi_3 > 0$ for SN/S/S; $\xi_r > 0$ and $\xi_3 < 0$ for UFC; and $\xi_r < 0$ and $\xi_3 > 0$ for SFS. On the plane $P > 0$ as shown in Fig. 10(b), the curves $r^{(1a)}$ and $r^{(1b)}$ are no longer symmetric to each other, and the curve $r^{(2)}$ intersects with the curve $r^{(1b)}$ at $Q = 0$ and $R = 0$. Six different topologies can be identified: UFC, UN/S/S, SN/S/S, SFS, SFC, and SN/SN/SN, which are denoted by $S^{(1)}$, $S^{(2)}$, $S^{(3)}$, $S^{(4)}$, $S^{(5)}$, and $S^{(6)}$, respectively. It is worth noting that $\xi_r < 0$ and $\xi_3 < 0$ for SFC, while $\xi_1 < 0$, $\xi_2 < 0$, and $\xi_3 < 0$ for SN/SN/SN.

TABLE IV. Description of acronyms of various flow topologies.

Sector	Acronym	Description
$S^{(1)}$	UFC	Unstable focus/compressing
$S^{(2)}$	UN/S/S	Unstable node/saddle/saddle
$S^{(3)}$	SN/S/S	Stable node/saddle/saddle
$S^{(4)}$	SFS	Stable focus/stretching
$S^{(5)}$	SFC	Stable focus/compressing
$S^{(6)}$	SN/SN/SN	Stable node/stable node/stable node
$S^{(7)}$	UFS	Unstable focus/stretching
$S^{(8)}$	UN/UN/UN	Unstable node/unstable node/unstable node

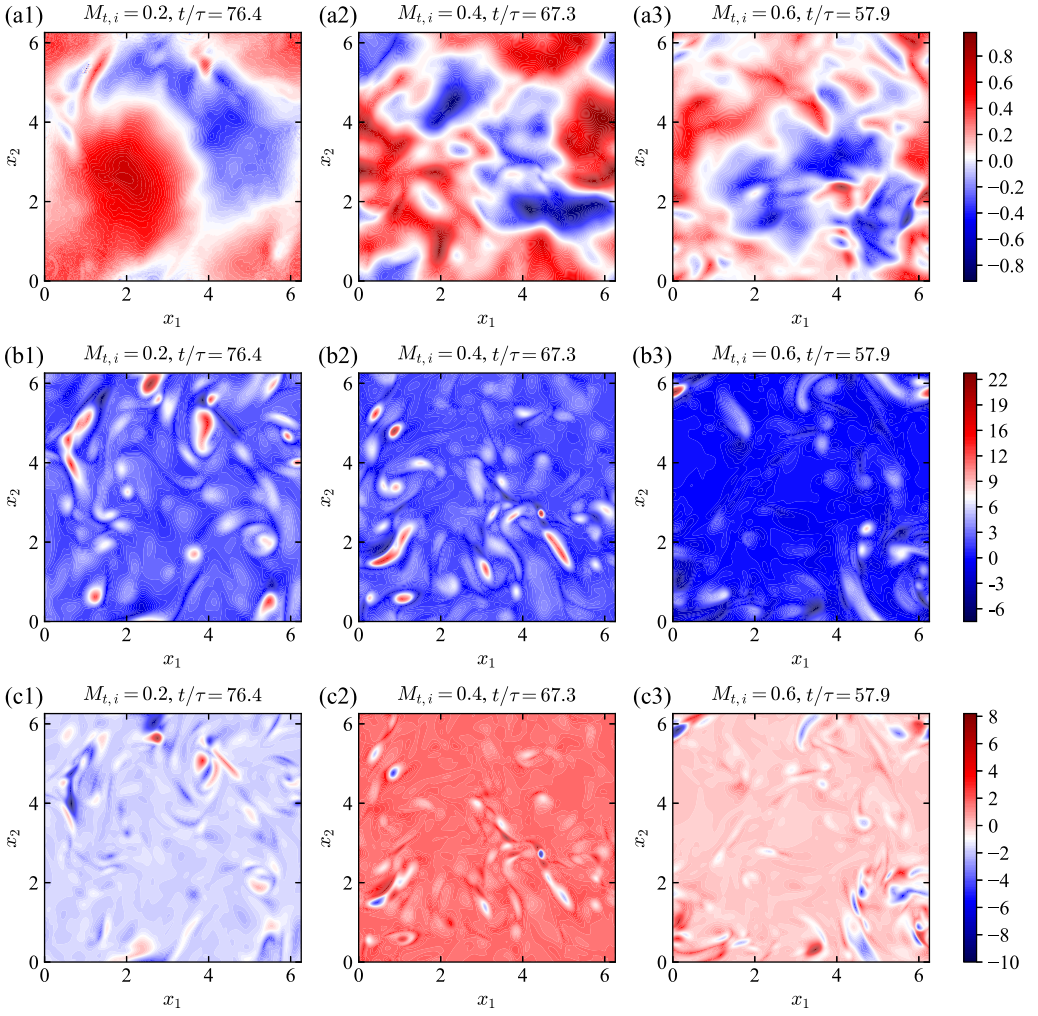

FIG. 11. Instantaneous contours of $P/\langle Q_w\rangle^{1/2}$, $Q/\langle Q_w\rangle$, and $R/\langle Q_w\rangle^{3/2}$ for the simulations with 256^3 grid resolution for $M_{t,i}=0.2$, 0.4, 0.6 at the maximum heat release time for each turbulent Mach number: (a1)–(a3) $P/\langle Q_w\rangle^{1/2}$; (b1)–(b3) $Q/\langle Q_w\rangle$; (c1)–(c3) $R/\langle Q_w\rangle^{3/2}$.

On the plane $P<0$ as shown in Fig. 10(c), the curve $r^{(2)}$ intersects with the curve $r^{(1a)}$ at $Q=0$ and $R=0$. Six different topologies can be identified: UFC, UN/S/S, SN/S/S, SFS, UFS, and UN/UN/UN, which are denoted by $S^{(1)}$, $S^{(2)}$, $S^{(3)}$, $S^{(4)}$, $S^{(7)}$, and $S^{(8)}$, respectively. It is worth noting that $\xi_r>0$ and $\xi_3>0$ for UFS, while $\xi_1>0$, $\xi_2>0$, and $\xi_3>0$ for UN/UN/UN.

2. Statistical properties of the invariants of velocity gradient tensor

We show instantaneous contours of normalized three invariants $P/\langle Q_w\rangle^{1/2}$, $Q/\langle Q_w\rangle$, and $R/\langle Q_w\rangle^{3/2}$ for $M_{t,i}=0.2$, 0.4, and 0.6 at the maximum heat release time for each turbulent Mach number in Fig. 11. The first invariant P characterizes the velocity divergence. As shown in Figs. 11(a1)–11(a3), a large number of compression and expansion patches are observed in the flow field. With the increase of initial turbulent Mach number, the length scales of the compression and expansion structures become smaller. The normalized second invariant $Q/\langle Q_w\rangle$ is shown in Figs. 11(b1)–11(b3). A number of small-scale positive $Q/\langle Q_w\rangle$ blobs are found in both compression

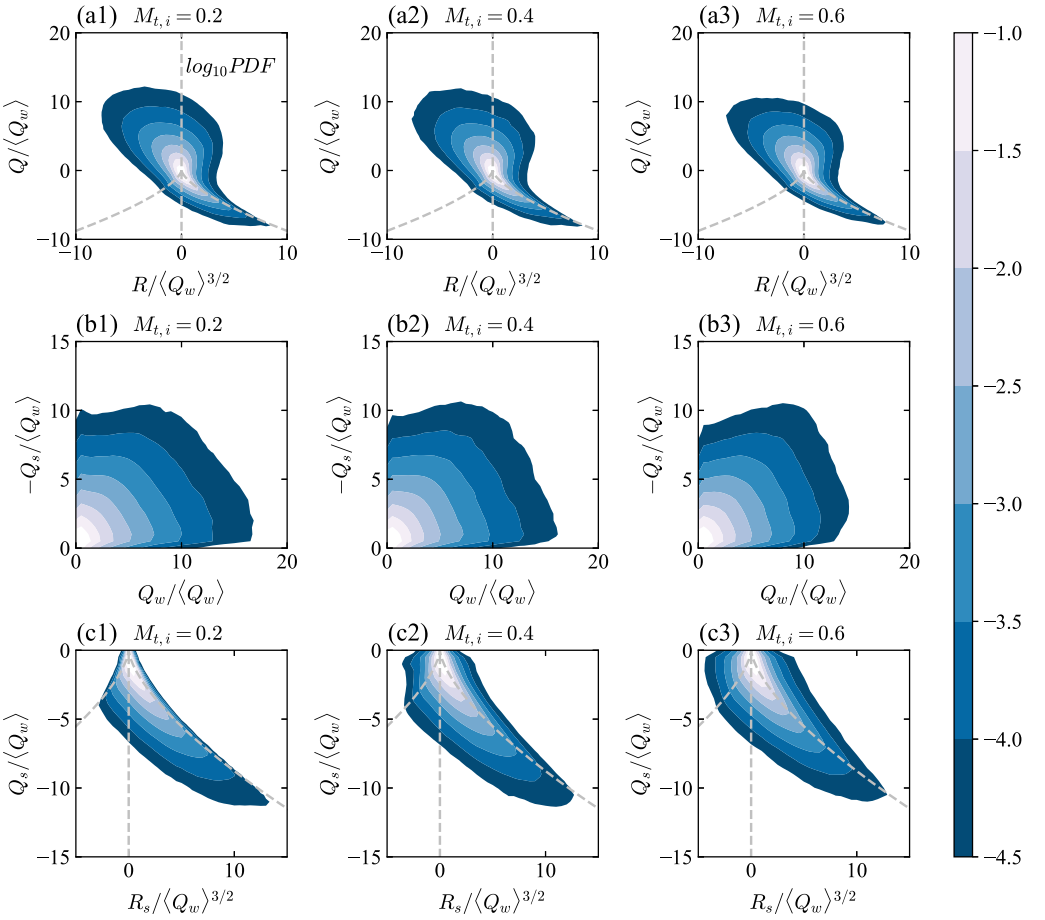

FIG. 12. Logarithm of the joint PDF of the second and third invariants of the velocity gradient tensor and their components at $M_{t,i} = 0.2$, 0.4, 0.6: (a1)–(a3) $\log_{10}\text{PDF}(Q, R)$, the second and third invariants are normalized as $Q/\langle Q_w \rangle$ and $R/\langle Q_w \rangle^{3/2}$, respectively; (b1)–(b3) $\log_{10}\text{PDF}(-Q_s, Q_w)$, the invariants are normalized as $-Q_s/\langle Q_w \rangle$ and $Q_w/\langle Q_w \rangle$, respectively; (c1)–(c3) Q_w $\log_{10}\text{PDF}(Q_s, R_s)$, the invariants are normalized as $Q_s/\langle Q_w \rangle$ and $R_s/\langle Q_w \rangle^{3/2}$, respectively. (a1), (b1), (c1) $M_{t,i} = 0.2$; (a2), (b2), (c2) $M_{t,i} = 0.4$; (a3), (b3), (c3) $M_{t,i} = 0.6$.

and expansion regions, indicating that flow dilatation has little influence on the flow areas in which the enstrophy dominates over stain. A large part of the flow field has a negative $Q/\langle Q_w \rangle$ value, suggesting that the strain dominates over enstrophy in most areas of the flow field. The third normalized invariant $R/\langle Q_w \rangle^{3/2}$ is shown in Fig. 11(c1)–11(c3). It is found that in positive $Q/\langle Q_w \rangle$ regions, smaller scale negative $R/\langle Q_w \rangle^{3/2}$ blob structures are found, indicating that the vortex stretching is dominating these areas.

The statistical properties of the velocity gradient tensor can be studied conveniently in terms of the joint PDF of the second and third invariants and their components. Figure 12 depicts the joint PDF of the normalized second and third invariants and their components averaged using simulated data in the strong reaction phase. The logarithm of the joint PDF of Q and R, $\log_{10}\text{PDF}(Q, R)$ is shown in Figs. 12(a1)–12(a3), where Q and R are normalized as $Q/\langle Q_w \rangle$ and $R/\langle Q_w \rangle^{3/2}$, respectively. It is shown that the joint PDF of the second and third invariants at three turbulent Mach numbers us consistent with the well-known universal teardrop diagrams [4]. Moreover, the diagram of the joint PDF of Q and R is insensitive to the change of turbulent Mach number. The joint PDF of

$-Q_s$ and Q_w can be utilized to identify the physical position relative to the vortex tube. Points close to the horizontal line ($-Q_s = 0$) implies a flow region at the center of the vortex with high enstrophy but small translational dissipation. Points close to the vertical line ($Q_w = 0$) suggest regions away from the vortex tubes having high translational dissipation but low enstrophy [64]. The logarithm of the joint PDF of $-Q_s$ and Q_w, $\log_{10}\text{PDF}(-Q_s, Q_w)$ is shown in Figs. 12(b1)–12(b3), where $-Q_s$ and Q_w are normalized as $-Q_s/\langle Q_w\rangle$ and $Q_w/\langle Q_w\rangle$, respectively. It is shown that the diagrams at three turbulent Mach numbers are similar to each other, suggesting that the physical position relative to the vortex tube is slightly influenced by turbulent Mach number, and the flow regions at the center of the vortex and away from the vortex tube are equally distributed. The logarithm of the joint PDF of Q_s and R_s, $\log_{10}\text{PDF}(Q_s, R_s)$ as shown in Figs. 12(c1)–12(c3) is another important invariant map related to the geometry of small-scale fluid strain, where Q_s and R_s are normalized as $Q_s/\langle Q_w\rangle$ and $R_s/\langle Q_w\rangle^{3/2}$, respectively. In particular, the positive values of the third invariant R_s indicate the flow compression and the destruction of strain, and the negative value of R_s suggests flow expansion and the production of strain. It is observed that the positive R_s dominates over the negative R_s at three turbulent Mach numbers, suggesting that the flow compression is the predominant flow motion. It also can be found that both the positive and the negative values of R_s increase with the increase of turbulent Mach number, suggesting that both strain production and destruction are enhanced with the increase of flow compressibility.

The statistical properties of velocity gradient tensor can be further analyzed in terms of the joint PDF of the second and third invariants PDF(Q, R) for a given range of velocity divergence θ. Three typical ranges of velocity divergence are considered: $-0.05 \leqslant \theta/\theta' \leqslant 0.05$, $-2.05 \leqslant \theta/\theta' \leqslant -1.95$, and $1.95 \leqslant \theta/\theta' \leqslant 2.05$, approximately corresponding to three values of the normalized first invariant $P/P' \approx 0$, $P/P' \approx 2$, and $P/P' \approx -2$, respectively. Here P' represents the r.m.s. value of the first invariant P: $P' = \sqrt{\langle P^2\rangle} = \theta'$. The second and third invariants of the velocity gradient tensor are normalized as $Q/\langle Q_w\rangle$ and $R/\langle Q_w\rangle^{3/2}$, respectively. Figure 13 depicts the logarithm of the joint PDF of the second and third invariants of the velocity gradient tensor at $M_{t,i} = 0.2$, 0.4, and 0.6 for three ranges of velocity divergence averaged using simulated data in the strong heat release phase. It is shown that the joint PDF for the nearly incompressible region $-0.05 \leqslant \theta/\theta' \leqslant 0.05$ ($P/P' \approx 0$) as shown in Figs. 13(a1)–13(a3) exhibits the teardrop shapes at three turbulent Mach numbers, which is similar to those observed in the overall flow field as shown in Fig. 12(a1)–12(a3), as well as reported results in the compressible decaying isotropic turbulence [65] and compressible turbulent boundary layer [24]. Similar observations were also reported in a wide range of incompressible turbulent flows [2,3,66]. The joint PDF of the second and third invariants at three turbulent Mach numbers in the compression region $-2.05 \leqslant \theta/\theta' \leqslant -1.95$ ($P/P' \approx 2$) as shown in Figs. 13(b1)–13(b3) becomes more symmetric, and the fractions of the joint PDF occupying the first and third quadrants become larger, as compared to those of the nearly incompressible region $-0.05 \leqslant \theta/\theta' \leqslant 0.05$. It is observed that the flow topologies $S^{(1)}$ and $S^{(4)}$ are predominant in the compression regions. The joint PDF of the second and third invariants at three turbulent Mach numbers in the expansion region $1.95 \leqslant \theta/\theta' \leqslant 2.05$ ($P/P' \approx -2$) as shown in Figs. 13(c1)–13(c3) has a tendency to occupy the second and fourth quadrants and exhibits more skewed shapes as compared to those of the nearly incompressible region $-0.05 \leqslant \theta/\theta' \leqslant 0.05$. It is found that the expansion region is favorable to the unstable topologies $S^{(2)}$ and $S^{(7)}$. It is worth noting that the joint PDFs for three ranges of velocity divergence are similar to each other at a given velocity divergence range, suggesting that flow compressibility exerts little influence on the dominating feature of the joint PDFs of the second and third invariants.

We denote three eigenvectors of the strain rate tensor S_{ij} as $\mathbf{\Lambda_1}$, $\mathbf{\Lambda_2}$, and $\mathbf{\Lambda_3}$, with corresponding eigenvalues λ_1, λ_2, and λ_3 arranged in ascending order: $\lambda_1 \leqslant \lambda_2 \leqslant \lambda_3$. The normalized eigenvalues of the strain rate tensor are defined as [30]:

$$\beta_j = \frac{\lambda_j}{\sqrt{\lambda_1^2 + \lambda_2^2 + \lambda_3^2}}. \tag{34}$$

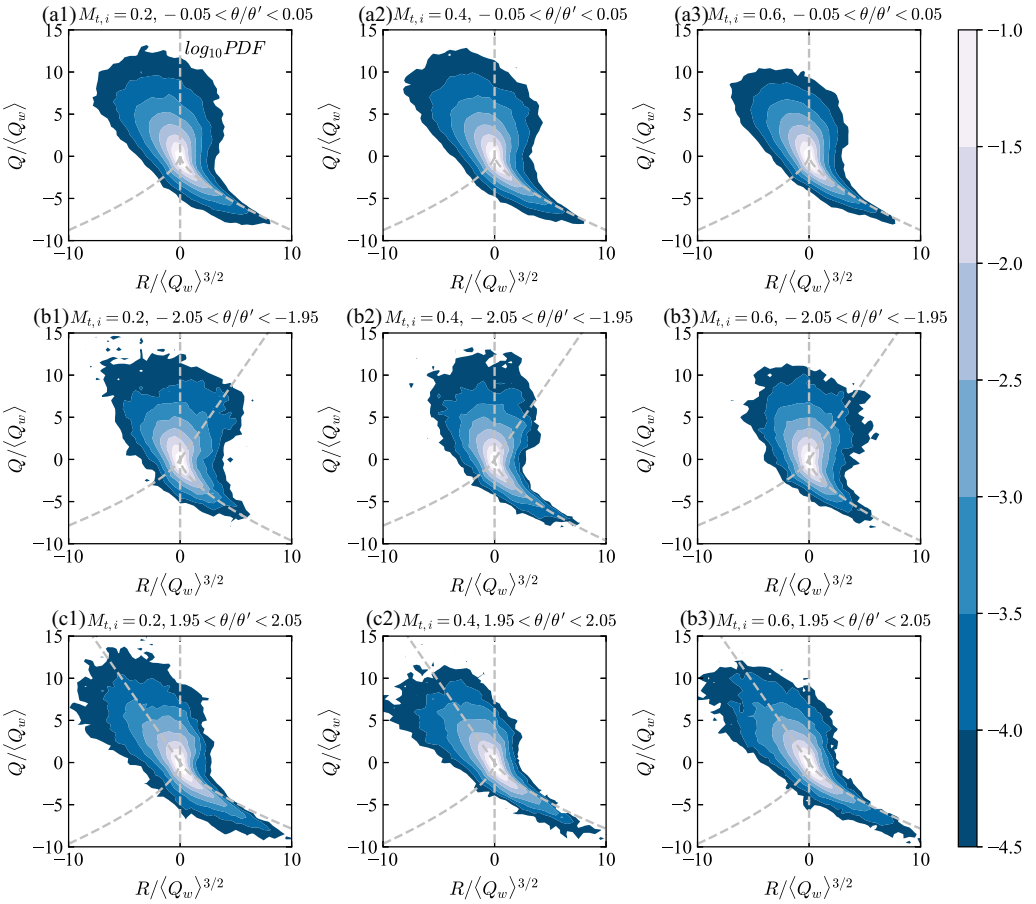

FIG. 13. Logarithm of the joint PDF of the second and third invariants of the velocity gradient tensor at $M_{t,i} = 0.2$, 0.4, 0.6, for three ranges of velocity divergence: (a1)–(a3) $-0.05 \leqslant \theta/\theta' \leqslant 0.05$; (b1)–(b3) $-2.05 \leqslant \theta/\theta' \leqslant -1.95$; (c1)–(c3) $1.95 \leqslant \theta/\theta' \leqslant 2.05$. (a1), (b1), (c1) $M_{t,i} = 0.2$; (a2), (b2), (c2) $M_{t,i} = 0.4$; (a3), (b3), (c3) $M_{t,i} = 0.6$. The second and third invariants are normalized as $Q/\langle Q_w \rangle$ and $R/\langle Q_w \rangle^{3/2}$, respectively.

We provide the PDFs of the normalized eigenvalues β_j of the strain rate tensor at $M_{t,i} = 0.2$, 0.4, and 0.6 averaged using simulated data in the strong heat release phase in Fig. 14. It is shown that shapes of PDF of the normalized eigenvalues are close to each other for three turbulent Mach numbers. Most values of β_1 are negative, and the maximum value of the PDF decreases with the increase of turbulent Mach number, while most values of β_2 and β_3 are positive. The most probable ratios of three eigenvalues for the strain rate tensor at three turbulent Mach numbers are very close to $-4{:}1{:}3$, which is similar to the most likely eigenvalue ratio in incompressible turbulence [18]. The observation suggests that due to heat release through chemical reactions, the flow compressibility is reduced to much lower values for each turbulent Mach number compared to their initial values. Thus the most probable ratios of three eigenvalues for the strain rate tensor at three turbulent Mach numbers are close to that observed in incompressible turbulence.

We further provide the conditional PDFs of the normalized eigenvalues β_j of the strain rate tensor conditioned on the normalized velocity divergence θ/θ' at $M_{t,i} = 0.2$, 0.4, and 0.6 averaged using simulated data in the strong heat release phase in Fig. 15. In high compression regions $-\infty < \theta/\theta' < -2$ as shown in Figs. 15(a), 15(c), and 15(e), the most probable values of β_j decrease slightly

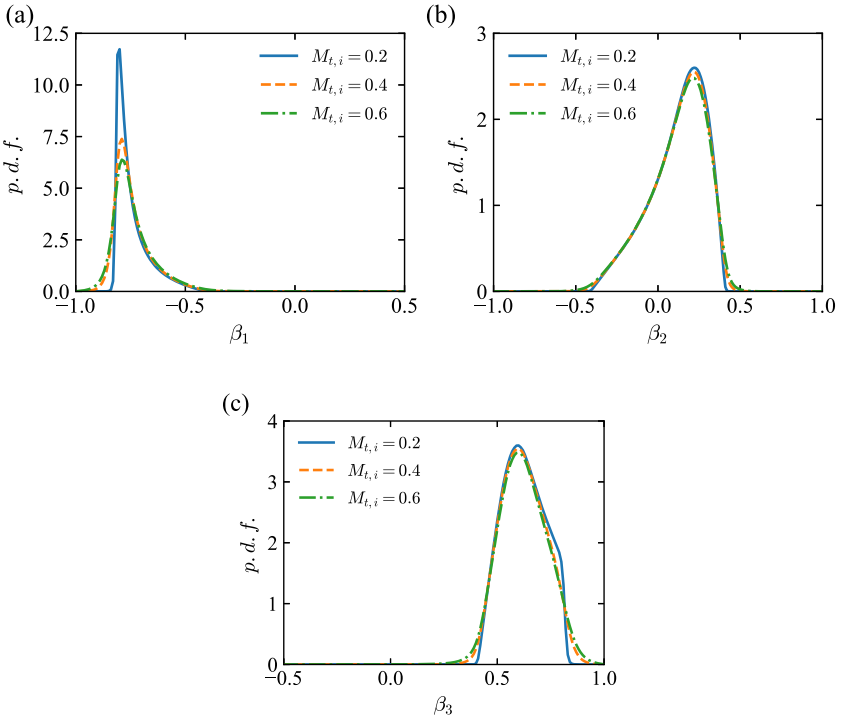

FIG. 14. PDFs of the normalized eigenvalues β_j of the strain rate tensor at $M_{t,i} = 0.2, 0.4, 0.6$.

with the increase of turbulent Mach number. In high expansion regions $2 < \theta/\theta' < +\infty$ as shown in Figs. 15(b), 15(d), and 15(f), the most probable values of β_j increase slightly with the increase of turbulent Mach number. The most probable ratios of three eigenvalues for the strain rate tensor at three turbulent Mach numbers are close to the overall probable ratio. The observation suggests that the strong heat release reduces flow compressibility characterized by the initial turbulent Mach number.

3. Flow topology and the relevant statistical properties

The statistical properties in *P*-*Q*-*R* space can be characterized conveniently by the volume fractions $V_f^{(k)}$ of various flow topologies $S^{(k)}$ in compressible isotropic turbulence. We show the volume fractions $V_f^{(k)}$ of various flow topologies at turbulent Mach numbers $M_{t,i} = 0.2$, 0.4, 0.6 for different Taylor Reynolds numbers averaged using simulated data in the strong heat release phase in Table V. It is observed that three topologies $S^{(1)}$, $S^{(2)}$, and $S^{(4)}$ are predominant flow patterns at $M_{t,i} = 0.2$, 0.4, and 0.6 for different Taylor Reynolds numbers, similar to the situations of decaying compressible isotropic turbulence [65] and the compressible turbulent boundary layer [24]. The results are consistent with the joint PDF of the second and third invariants as shown in Figs. 12(a1)–12(a3), in which values predominate in the first, second, and fourth quadrants. The topologies $S^{(5)}$, $S^{(6)}$, $S^{(7)}$, and $S^{(8)}$ can be observed only for compressible flows. The volume fractions of topologies $S^{(6)}$ and $S^{(8)}$ are very small as compared to those of $S^{(5)}$ and $S^{(7)}$. It is noted that the flow topologies $S^{(5)}$ and $S^{(7)}$ become larger with the increase of turbulent Mach number. The Taylor Reynolds number has little influence on the volumetric average of flow topology statistics.

To further evaluate the heat release effects on volume fractions of various flow topologies, Fig. 16 shows the relative values of volume fractions of various flow topologies in three reaction phases. The volume fractions of topologies $S^{(1)}$ to $S^{(8)}$ in three reaction phases are normalized by the

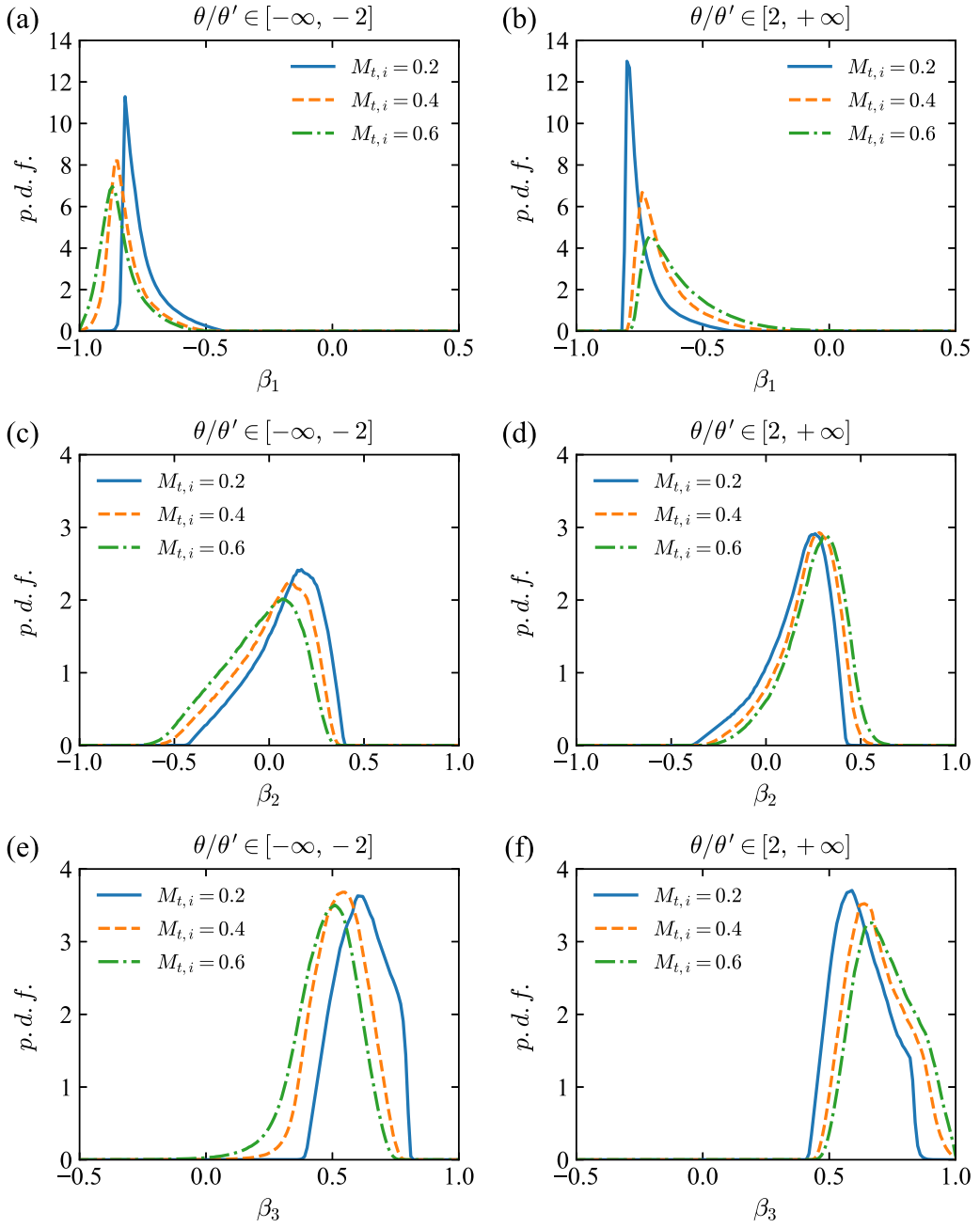

FIG. 15. Conditional PDFs of the normalized eigenvalues β_j of the strain rate tensor at $M_{t,i} = 0.2, 0.4, 0.6$, for two ranges of velocity divergence: (a), (c), (e) $-\infty < \theta/\theta' < -2$; (b), (d), (f) $2 < \theta/\theta' < +\infty$.

corresponding values in the initial reaction phase. Thus, the relative values of volume fraction of various flow topologies are 1.0 in the initial reaction phase. It is shown that the relative values of the volume fraction of topologies $S^{(1)} \sim S^{(4)}$ are close to each other in three reaction phases at three initial Taylor Reynolds numbers. The relative values of volume fraction of topologies $S^{(5)}$ and $S^{(7)}$ significantly increase in the strong heat release phase, both of which are focal topologies,

TABLE V. Volume fractions of various flow topologies (%).

Resolution	Re_i	$M_{t,i}$	$S^{(1)}$	$S^{(2)}$	$S^{(3)}$	$S^{(4)}$	$S^{(5)}$	$S^{(6)}$	$S^{(7)}$	$S^{(8)}$
64^3	34	0.17	29.44	25.40	6.88	38.19	0.07	0.00	0.03	0.00
64^3	34	0.34	28.89	23.54	6.49	40.68	0.27	0.00	0.13	0.00
64^3	34	0.51	27.46	23.83	6.84	37.78	1.19	0.00	0.90	0.00
128^3	62	0.18	25.85	27.75	7.37	38.89	0.09	0.00	0.05	0.00
128^3	62	0.36	25.18	27.68	7.45	37.18	1.35	0.00	1.17	0.00
128^3	63	0.54	24.26	26.28	7.82	35.99	2.57	0.01	3.06	0.01
256^3	99	0.20	24.47	29.59	8.45	36.92	0.30	0.00	0.27	0.00
256^3	100	0.40	23.69	28.78	8.34	36.25	1.45	0.00	1.48	0.00
256^3	101	0.60	23.11	28.18	8.43	35.65	2.15	0.00	2.39	0.00

suggesting that the strong heat release is more likely to enhance the flow topologies which are sensitive to dilatation change. This observation is consistent with the results obtained by Lai *et. al* [67] in simulating a turbulent premixed flame in which the volume fraction of focal topologies decreases from the unburned side to the burned side of the flame front.

In order to address the effect of flow topology on the enstrophy production $\omega_i\omega_j S_{ij}$, we calculate the percentages of the relative contribution of various flow topologies to the average enstrophy production as shown in Table VI. The statistics are averaged using simulated data in the strong heat release phase. It is found that the total percentage of relative contribution of topologies $S^{(2)}$ and $S^{(4)}$ is larger than 90% at three turbulent Mach numbers, indicating that the topologies $S^{(2)}$ and $S^{(4)}$ have major contributions to the average enstrophy production $\langle\omega_i\omega_j S_{ij}\rangle$. This observation is consistent with the teardrop shapes of PDF(Q, R), which exhibit a statistical preference in the second and fourth quadrants of Q-R space corresponding to the topologies $S^{(2)}$ and $S^{(4)}$. The contribution of topology $S^{(1)}$ to the average enstrophy production is negative for all turbulent Mach numbers,

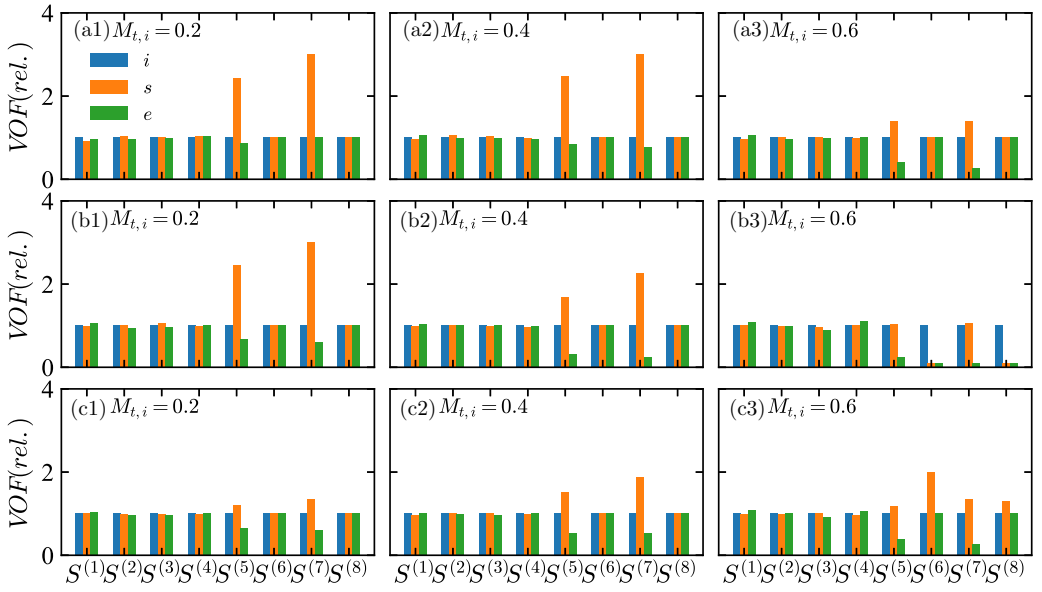

FIG. 16. Relative values of volume fractions of various flow topologies in three reaction phases, (a1)–(a3) results obtained by 64^3 simulation data; (b1)–(b3) results obtained by 128^3 simulation data; (c1)–(c3) results obtained by 256^3 simulation data.

TABLE VI. Percentages of relative contribution of various flow topologies to the average enstrophy production $\langle \omega_i \omega_j S_{ij} \rangle$ (%).

Resolution	Re_i	$M_{t,i}$	$S^{(1)}$	$S^{(2)}$	$S^{(3)}$	$S^{(4)}$	$S^{(5)}$	$S^{(6)}$	$S^{(7)}$	$S^{(8)}$
64^3	34	0.17	−12.28	20.16	4.38	87.73	0.00	0.00	0.00	0.00
64^3	34	0.34	−7.77	20.56	4.58	82.07	0.00	0.00	0.02	0.00
64^3	34	0.51	−10.21	27.34	4.70	85.43	−0.24	0.00	0.27	0.00
128^3	62	0.18	−4.82	23.02	4.33	77.46	0.01	0.00	0.01	0.00
128^3	62	0.36	−5.10	22.29	4.18	78.43	−0.22	0.00	0.43	0.00
128^3	63	0.54	−2.15	24.55	4.07	72.36	−1.31	0.00	2.49	0.00
256^3	99	0.20	−5.36	22.77	4.26	78.28	−0.01	0.00	0.06	0.00
256^3	100	0.40	−4.52	23.17	4.22	76.81	−0.32	0.00	0.63	0.00
256^3	101	0.60	−3.84	23.73	4.18	75.19	−0.90	0.00	1.64	0.00

suggesting that the topology $S^{(1)}$ trends to lead to the destruction of enstrophy. The contribution of topology $S^{(5)}$ and $S^{(7)}$ to enstrophy production is the opposite. With the increase of turbulent Mach number, the enstrophy production by topology $S^{(7)}$ increases.

Figure 17 shows the relative contribution of various flow topologies to the average enstrophy production $\langle \omega_i \omega_j S_{ij} \rangle$ in three reaction phases. The relative contribution of various flow topologies to the average enstrophy production in three reaction phases is normalized by the corresponding values in the initial reaction phase. It is observed that the destruction of topology $S^{(1)}$ to the average enstrophy slightly decreases, while the contribution of topology $S^{(7)}$ to the average enstrophy production significantly increases in the strong heat release phase. Heat release leads to the increase of the relative volume fraction of flow topologies $S^{(5)}$ and $S^{(7)}$ in the strong heat release phase as shown in Fig. 16; however, the effect of the relative increased volume fraction of topology $S^{(5)}$ to the average enstrophy is not evident compared that of topology $S^{(7)}$. This observation suggests that

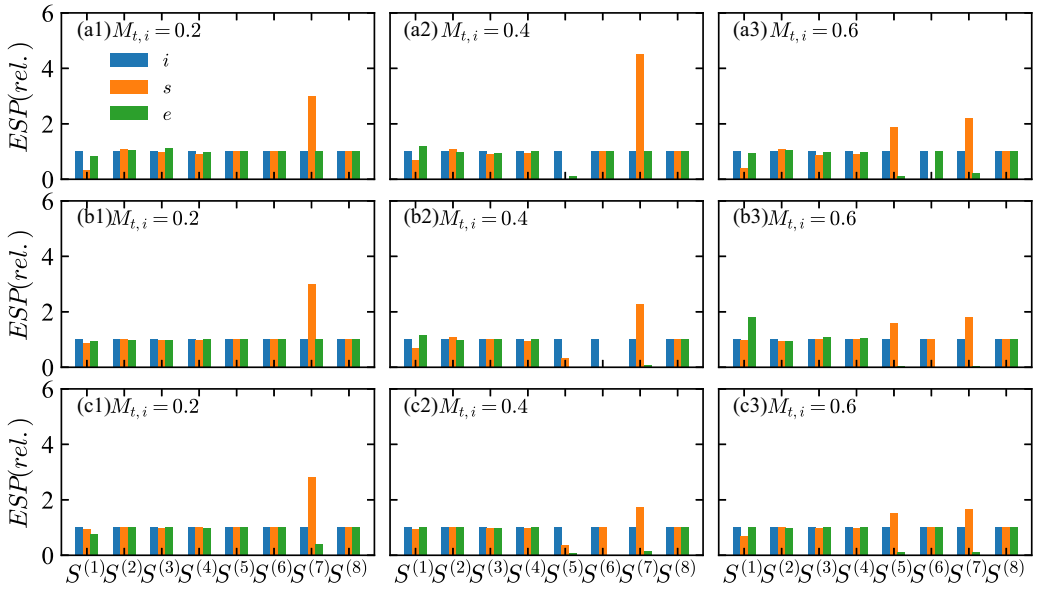

FIG. 17. Relative contribution of various flow topologies to the average enstrophy production $\langle \omega_i \omega_j S_{ij} \rangle$ in three reaction phases: (a1)–(a3) results obtained by 64^3 simulation data; (b1)–(b3) results obtained by 128^3 simulation data; (c1)–(c3) results obtained by 256^3 simulation data.

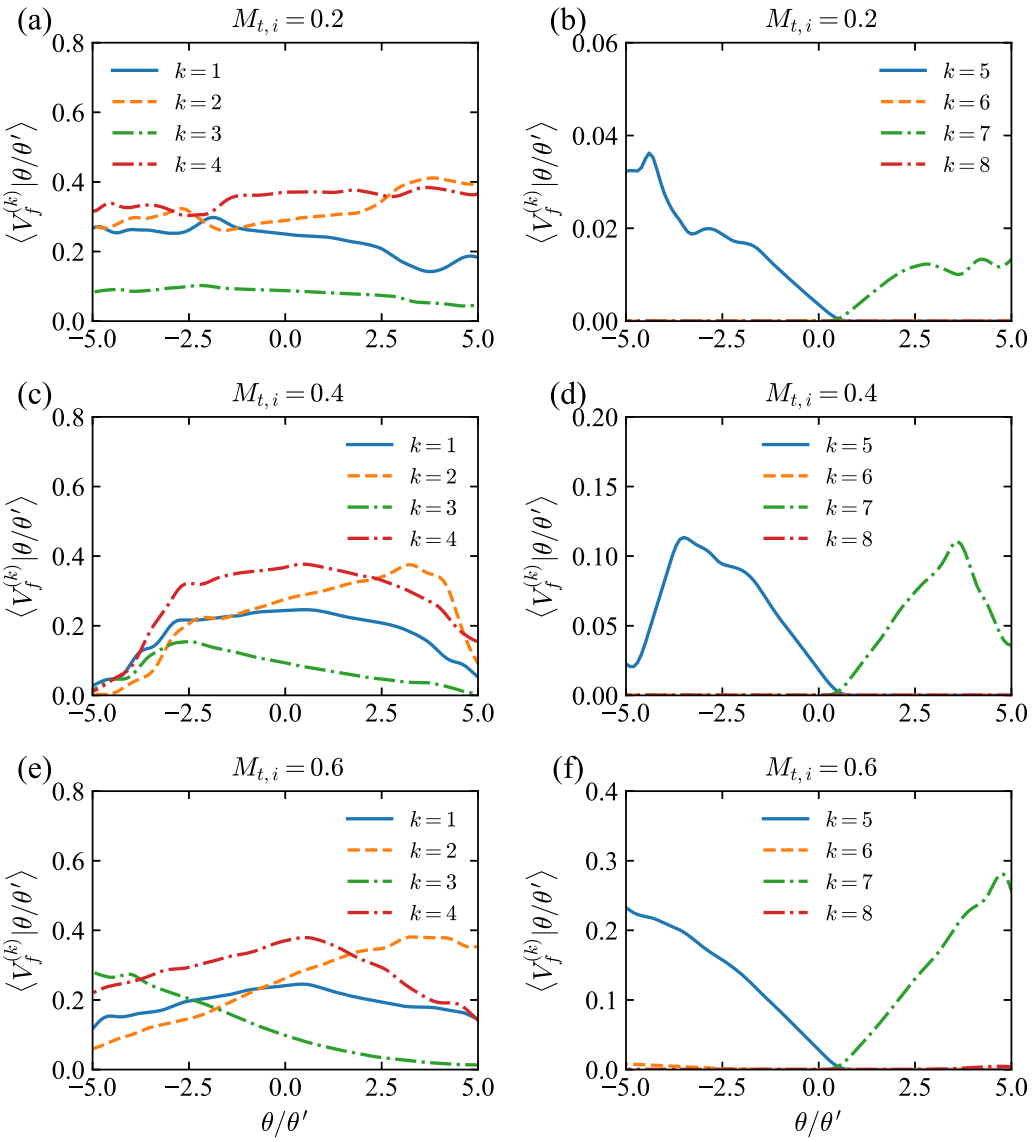

FIG. 18. Volume fractions $V_f^{(k)}$ of various flow topologies $S^{(k)}$ conditioned on the normalized velocity divergence θ/θ': (a), (b) $M_{t,i} = 0.2$; (c), (d) $M_{t,i} = 0.4$; (e), (f) $M_{t,i} = 0.6$.

the unstable focus/stretching topology enhanced by heat release is more conducive for enstrophy production.

We depict volume fractions $V_f^{(k)}$ of various flow topologies $S^{(k)}$ conditioned on the normalized velocity divergence at $M_{t,i} = 0.2$, 0.4, and 0.6 in Fig. 18. For compression regions $\theta/\theta' < 0$, as the magnitude of velocity divergence becomes larger, the volume fraction of the flow topology $S^{(3)}$ increases, while the volume fractions of the flow topologies $S^{(1)}$, $S^{(2)}$, and $S^{(4)}$ decrease. The flow topology $S^{(3)}$ predominates over seven other flow topologies in high compression regions $\theta/\theta' < -5$ at $M_{t,i}$= 0.2. It is shown that the volume fraction of the flow topology $S^{(5)}$ is comparable to or larger than those of flow topologies $S^{(1)}$, $S^{(2)}$, and $S^{(4)}$ in compression regions $\theta/\theta' < 0$ at $M_{t,i}$= 0.4 and 0.6. At $M_{t,i}$= 0.2, the volume fraction of the flow topology $S^{(6)}$ is larger than those of flow topologies

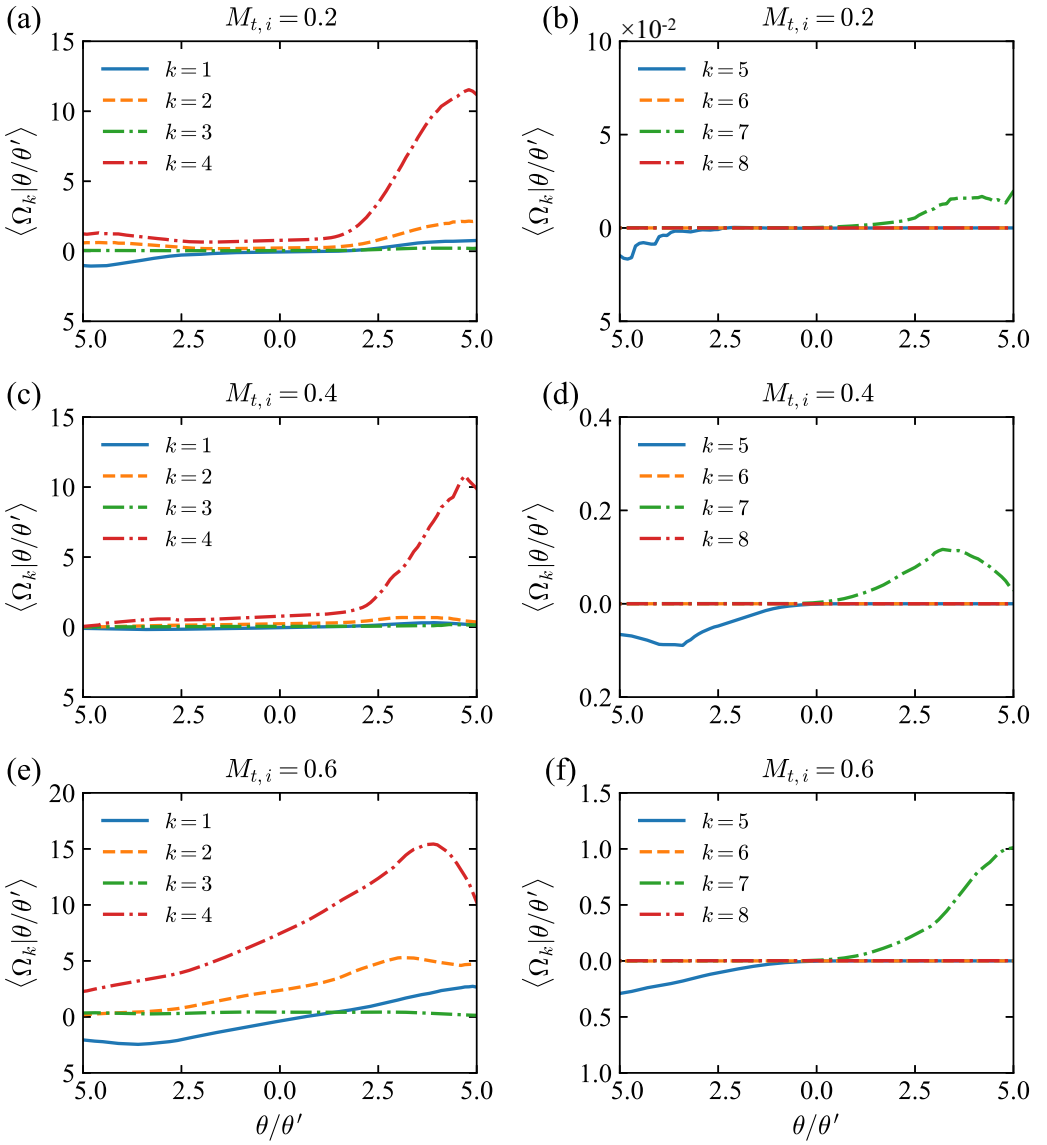

FIG. 19. The average of contributions Ω_k of various flow topologies $S^{(k)}$ to the normalized enstrophy production $\omega_i\omega_j S_{ij}/\langle\omega_i\omega_j S_{ij}\rangle$ conditioned on the normalized velocity divergence: (a), (b) $M_{t,i} = 0.2$; (c), (d) $M_{t,i} = 0.4$; (e), (f) $M_{t,i} = 0.6$.

$S^{(1)}$, $S^{(2)}$, $S^{(4)}$, and $S^{(5)}$ in high compression regions $\theta/\theta' < -2$. For expansion regions $\theta/\theta' > 0$, as the magnitude of velocity divergence increases, the volume fractions of the flow topologies $S^{(1)}$, $S^{(2)}$, $S^{(3)}$, and $S^{(4)}$ decrease. The volume fraction of the flow topology $S^{(2)}$ is larger than those of flow topologies $S^{(1)}$, $S^{(3)}$, and $S^{(4)}$ in high expansion regions $\theta/\theta' > 3$. It is found that the flow topology $S^{(7)}$ increases rapidly with the increase of velocity divergence in expansion regions $\theta/\theta' > 0$, and predominates over other seven flow topologies in expansion regions $\theta/\theta' > 0$ at $M_{t,i} = 0.4$ and 0.6. It should be noted that the volume fraction of the flow topology $S^{(8)}$ predominates over seven other flow topologies in expansion regions $\theta/\theta' > 0$ at $M_{t,i} = 0.2$. The volume fractions of the flow

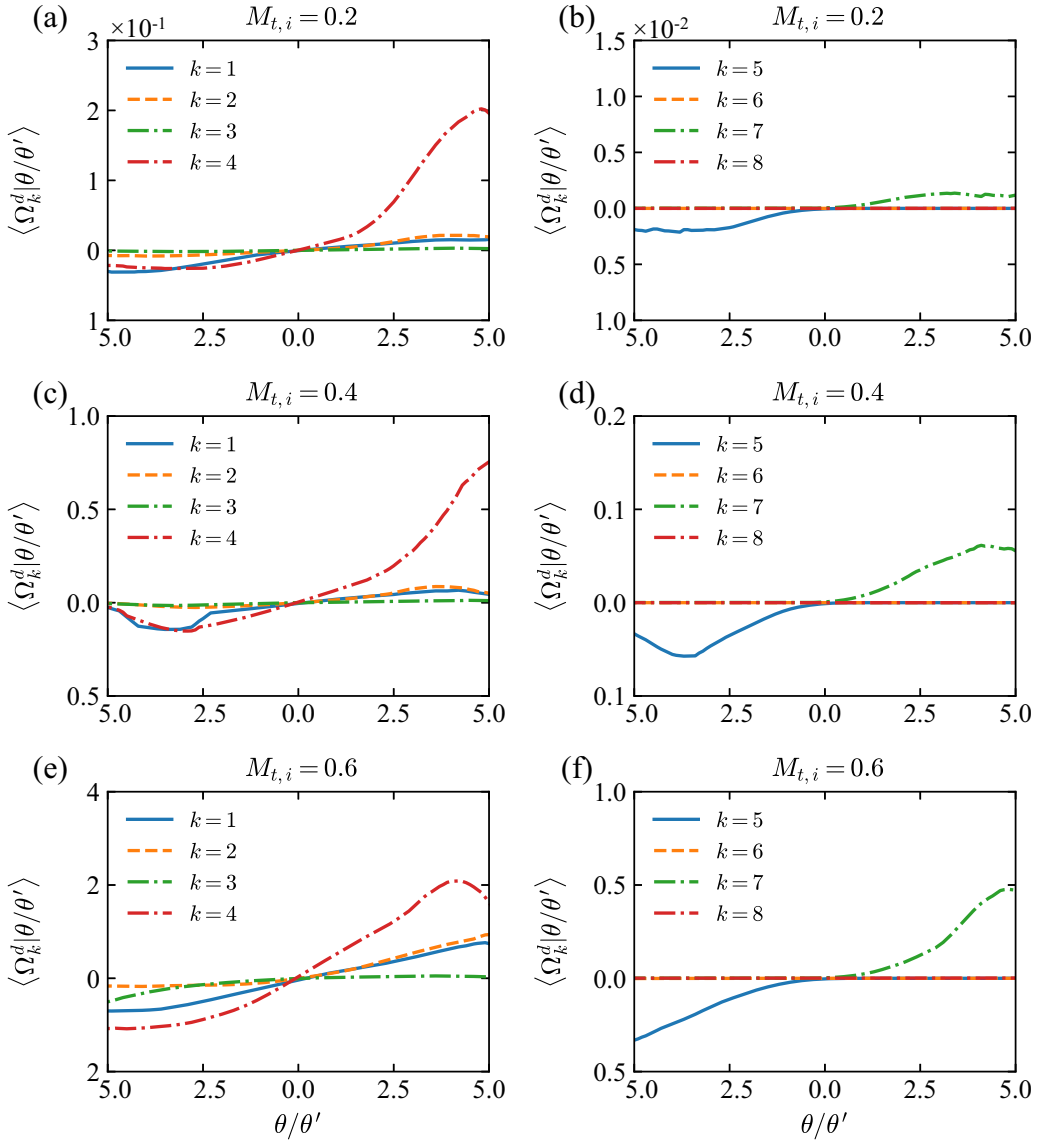

FIG. 20. The average of contributions Ω_k^d of various flow topologies $S^{(k)}$ to the normalized enstrophy production $\omega_i\omega_j S_{ij}^d/\langle\omega_i\omega_j S_{ij}\rangle$ conditioned on the normalized velocity divergence: (a), (b) $M_{t,i} = 0.2$; (c), (d) $M_{t,i} = 0.4$; (e), (f) $M_{t,i} = 0.6$.

topology $S^{(8)}$ at $M_{t,i} = 0.4$ and 0.6 are quite small compared to that at $M_{t,i} = 0.2$ in expansion regions.

We define the contributions Ω_k of various flow topologies $S^{(k)}$ to the normalized enstrophy production $\omega_i\omega_j S_{ij}/\langle\omega_i\omega_j S_{ij}\rangle$ as follows: $\Omega_k = \omega_i\omega_j S_{ij}/\langle\omega_i\omega_j S_{ij}\rangle$ if the point is located in the topology $S^{(k)}$; otherwise, Ω_k=0. Similarly, the contributions Ω_k^d of various flow topologies $S^{(k)}$ to the dilatational component of normalized enstrophy production $\omega_i\omega_j S_{ij}^d/\langle\omega_i\omega_j S_{ij}\rangle$ are defined as $\Omega_k^d = \omega_i\omega_j S_{ij}^d/\langle\omega_i\omega_j S_{ij}\rangle$ if the point is located in the topology $S^{(k)}$; otherwise, Ω_k^d=0. We plot the average of contributions Ω_k of various flow topologies $S^{(k)}$ to the normalized enstrophy production

$\omega_i\omega_j S_{ij}/\langle\omega_i\omega_j S_{ij}\rangle$ conditioned on the normalized velocity divergence at $M_{t,i} = 0.2$, 0.4, and 0.6 in Fig. 19. The statistics are averaged using simulated data in the strong heat release phase. In compression regions $\theta/\theta' < 0$, as the magnitude of velocity divergence becomes larger, the magnitudes of the conditional average of Ω_2 and Ω_4 are negligibly small, while the magnitudes of the conditional average of Ω_5 increases at $M_{t,i} = 0.2$ and 0.4. With the increase of turbulent Mach number, the magnitude of the conditional average of Ω_1, Ω_4, and Ω_5 become larger in compression regions at $M_{t,i} = 0.6$. In expansion regions $\theta/\theta' > 0$, the contribution of flow topologies $S^{(4)}$ and $S^{(7)}$ has significant contributions to the positive values of enstrophy production for $\theta/\theta' > 2.5$. Additionally, the contribution of topologies $S^{(3)}$, $S^{(6)}$, and $S^{(8)}$ to the enstrophy production is nearly zero in both compression and expansion regions. With increase of turbulent Mach number, the magnitudes of the conditional average of Ω_5 and Ω_7 increase due to the increase of flow compressibility.

We show the average of contributions Ω_k^d of various flow topologies $S^{(k)}$ to the dilatational component of normalized enstrophy production $\omega_i\omega_j S_{ij}^d/\langle\omega_i\omega_j S_{ij}\rangle$ conditioned on the normalized velocity divergence at $M_{t,i} = 0.2$, 0.4, and 0.6 in Fig. 20. The statistics are averaged using simulated data in the strong heat release phase. In compression regions $\theta/\theta' < 0$, the magnitudes of the conditional average of Ω_2^d and Ω_3^d are small, while the magnitudes of the conditional average of Ω_1^d, Ω_4^d, and Ω_5^d increase with the increase of magnitude of velocity divergence. In expansion regions $\theta/\theta' > 0$, the contribution of flow topologies $S^{(3)}$, $S^{(6)}$, and $S^{(8)}$ to the dilatational component of enstrophy production is negligible at three turbulent Mach numbers, while flow topologies $S^{(4)}$ have significant contributions to the positive values of the compressible component of enstrophy production. Comparatively, the contributions of topologies $S^{(4)}$ and $S^{(7)}$ to the dilatational component of enstrophy production are small compared to the contribution to the overall enstrophy production.

V. CONCLUDING REMARKS

In this paper, the statistical properties of flow topologies and enstrophy production in chemically reacting compressible isotropic turbulence are investigated at initial turbulent Mach numbers from 0.2 to 0.6 and at initial Taylor Reynolds number ranging from 32 to 160. During the chemical reaction process, the dynamic process of energy transfer leads to an increase of internal energy and a decrease of kinetic energy, as well as a decrease of flow compressibility and an increase of turbulent length scales.

The strong compression motions cause the destruction of enstrophy by the interaction between the vorticity and strain rate tensor, while strong expansion motions significantly enhance the generation of enstrophy by the interaction between the vorticity and strain rate tensor. The effects of compression and expansion motions on the enstrophy production are stronger at higher turbulent Mach numbers due to the larger compressibility after the strong heat release period during the chemical reaction process. The joint PDFs of the second and third invariants of velocity gradient tensor are similar to the well-known universal teardrop diagram at three turbulent Mach numbers. The joint PDF exhibits a skewed shape and has a stronger preference for the second and fourth quadrants in expansion regions and consequently leads to the enstrophy production. The three eigenvalues of the strain rate tensor have a most probable ratio of −4:1:3 at three turbulent Mach numbers, which is consistent with the results obtained in incompressible turbulence.

Various statistical properties of eight flow topologies based on the three invariants of the velocity gradient tensor are investigated. It is found that three flow topologies UFC, UN/S/S, and SFS are predominant flow patterns at three turbulent Mach numbers. The volume fractions of various flow topologies conditioned on the normalized velocity divergence are studied. It is revealed that the flow topology SFS predominates in high compression regions, while the flow topology UN/S/S predominates in high expansion regions at three turbulent Mach numbers. The various flow topologies exhibit different effects on the enstrophy production by the interaction between the vorticity and strain rate tensor. The topologies UN/S/S and SFS have major contributions to the overall positive enstrophy production. The contribution of topologies UFC and SFC to the average enstrophy production is negative at three turbulent Mach numbers.

In the current study we simulate the unsteady H_2/O_2 chemical reaction process, which includes the initial slow reaction phase, strong heat release phase, and slow reaction phase approaching the depletion of reactants. The temporally averaged flow quantities conditioned on the strong heat release phase reveals the distinct effects of reaction heat release on compressible turbulence, and those effects would pertain in quasistable premixed/nonpremixed turbulent combustion in regions where strong heat release prevails. To enhance the general applicability of the present methods and results for the H_2/O_2 reaction in compressible turbulence over a wide range of initial conditions, we provide the statistics of additional DNS data using a 64^3 grid for different initial pressure, temperature, and species mass fractions in Appendix B. Those additional statistics can be used to confirm the similarity of the temporal average of flow statistics conditioned on different reaction phases at different initial conditions.

ACKNOWLEDGMENTS

This work was supported by the National Natural Science Foundation of China (NSFC Grants No. 91952104, No. 92052301, No. 12172161, No. 12161141017, and No. 91752201), by the National Numerical Wind Tunnel Project (No. NNW2019ZT1-A04), by the NSFC Basic Science Center Program (Grant No. 11988102), by the Shenzhen Science and Technology Program (Grant No. KQTD20180411143441009), by the Key Special Project for Introduced Talents Team of Southern Marine Science and Engineering Guangdong Laboratory (Guangzhou) (Grant No. GML2019ZD0103), by the Department of Science and Technology of Guangdong Province (No. 2020B1212030001), and by the Guangdong Basic and Applied Basic Research Foundation (No. 2021A1515110845). This work was also supported by the Center for Computational Science and Engineering of the Southern University of Science and Technology.

APPENDIX A: VALIDATION OF CHEMICAL MODELING

In order to validate the chemical modeling, the zero-dimensional chemical reaction model based on dimensional variables is derived. The dimensional governing equations are given as follows, and the superscript "D" denotes dimensional variables. The zero-dimensional chemical reaction model is derived based on Navier-Stokes (N-S) equations without consideration of flow motion and diffusion [35]. The chemical reaction-related parameters, i.e., the reaction rate and heat of reaction in the zero-dimensional model, are identical to those used in solving chemically reacting compressible N-S equations:

$$\frac{\partial \rho^D}{\partial t^D} = 0, \tag{A1}$$

$$\frac{\partial \mathcal{E}^D}{\partial t^D} = -\sum_{s=1}^{n_s} H_s^{0,D} \dot{\omega}_s^D, \tag{A2}$$

$$\frac{\partial (\rho^D Y_s)}{\partial t^D} = \dot{\omega}_s^D, \quad s = 1, 2, \ldots, n_s - 1, \tag{A3}$$

$$p^D = \rho^D R^D T^D = \rho^D \frac{\mathbb{R}}{\mathbb{M}^D} T^D, \quad \mathcal{E}^D = \rho^D C_v^D T^D, \tag{A4}$$

$$\frac{1}{\mathbb{M}^D} = \sum_{s=1}^{n_s} \frac{Y_s}{\mathbb{M}_s^D}, \quad C_v^D = \sum_{s=1}^{n_s} Y_s C_{v,s}^D, \quad C_{v,s}^D = C_{p,s}^D - \frac{\mathbb{R}}{\mathbb{M}_s^D}, \tag{A5}$$

$$C_{p,s}^D = \frac{\mathbb{R}}{\mathbb{M}_s^D} [\zeta_{0,s} + \zeta_{1,s} T^D + \zeta_{2,s} (T^D)^2 + \zeta_{3,s} (T^D)^3 + \zeta_{4,s} (T^D)^4]. \tag{A6}$$

In the equations, the variables include density ρ, time t, pressure p, temperature T, total energy per unit volume $\mathcal{E}$, total number of species n_s, mass fraction of sth species Y_s, heat of reaction of sth

TABLE VII. Initial conditions for chemical modeling validation.

Case No.	H_2 (%)	O_2 (%)	N_2 (%)	T_{init} (K)	p_{init} (Pa)
S13	0.95	0.49	98.56	934	306002
S14	1.01	0.52	98.47	933	344505
S15	1.01	0.52	98.47	934	607950
S16	0.50	0.50	99.00	880	32424

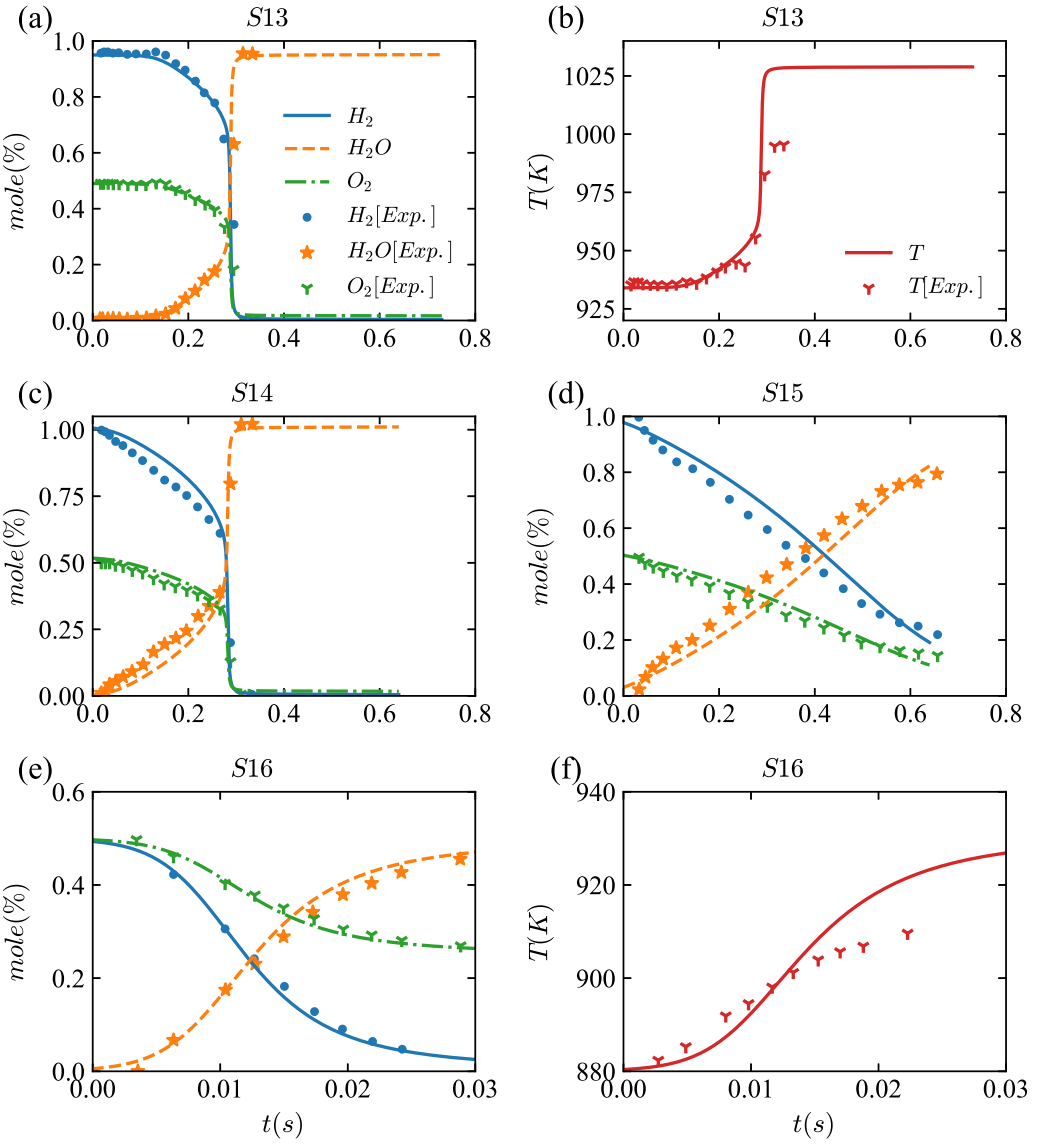

FIG. 21. Chemical modeling validation: temporal variation of species mole fractions and temperature for different initial conditions.

TABLE VIII. Initial conditions for chemical reactions.

Reaction No.	H_2 (%)	O_2 (%)	N_2 (%)	T_{init} (K)	p_{init} (Pa)
R1	16.0	8.00	76.00	880	32 424.0
R2	16.0	40.0	44.00	800	10 132.5
R3	10.0	20.0	70.00	1000	101 325.0
R4	5.00	5.00	90.00	1200	202 650.0

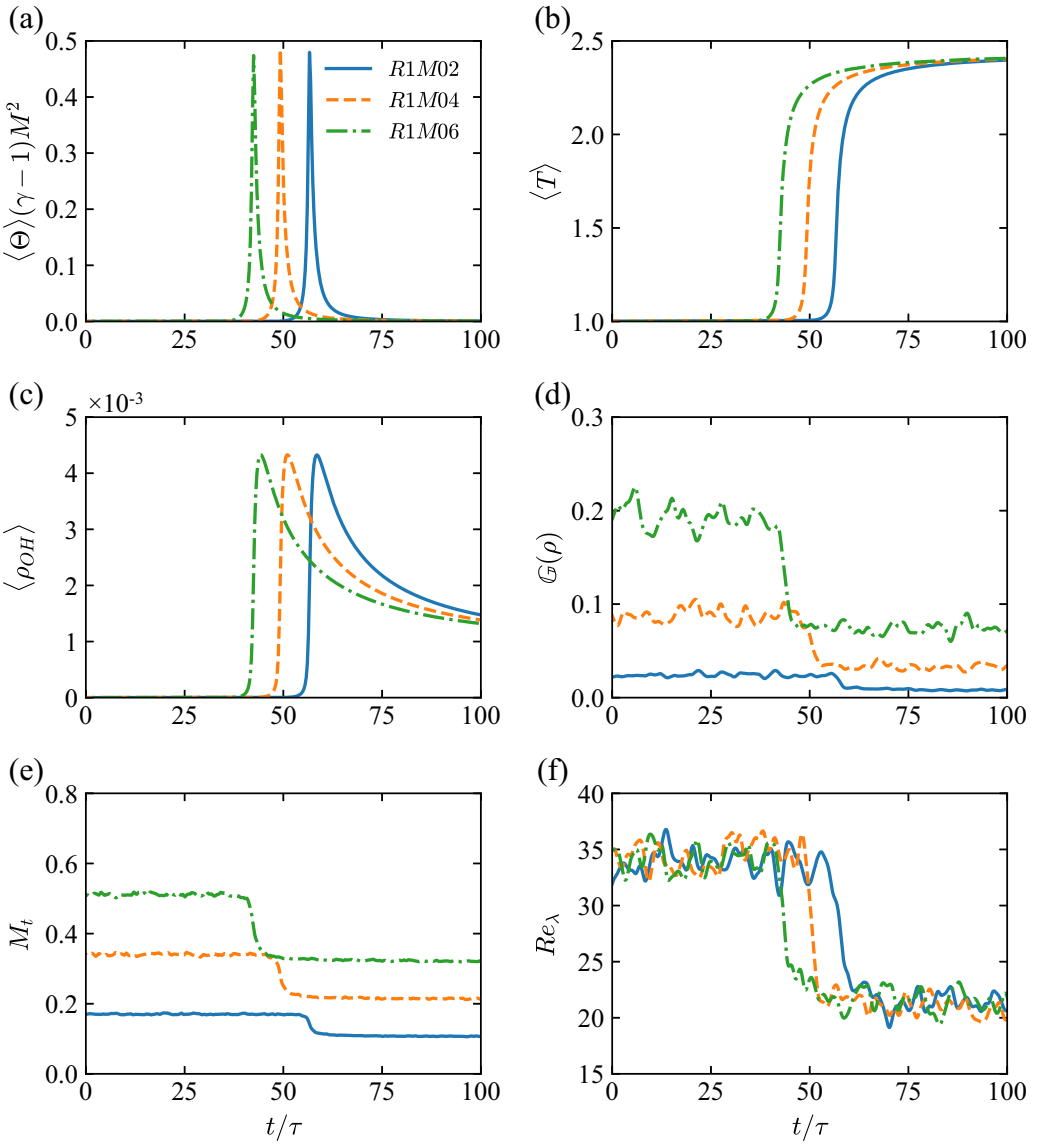

FIG. 22. Temporal variation of flow statistics of R1 at $M_{t,i} = 0.2, 0.4, 0.6$: (a) normalized averaged heat release $\langle\Theta\rangle(\gamma-1)M^2$; (b) averaged temperature $\langle T\rangle$; (c) averaged density of species OH $\langle\rho_{\text{OH}}\rangle$; (d) averaged magnitude of density gradient $\mathbb{G}(\rho)$; (e) turbulent Mach number M_t; (f) Taylor Reynolds number Re_λ.

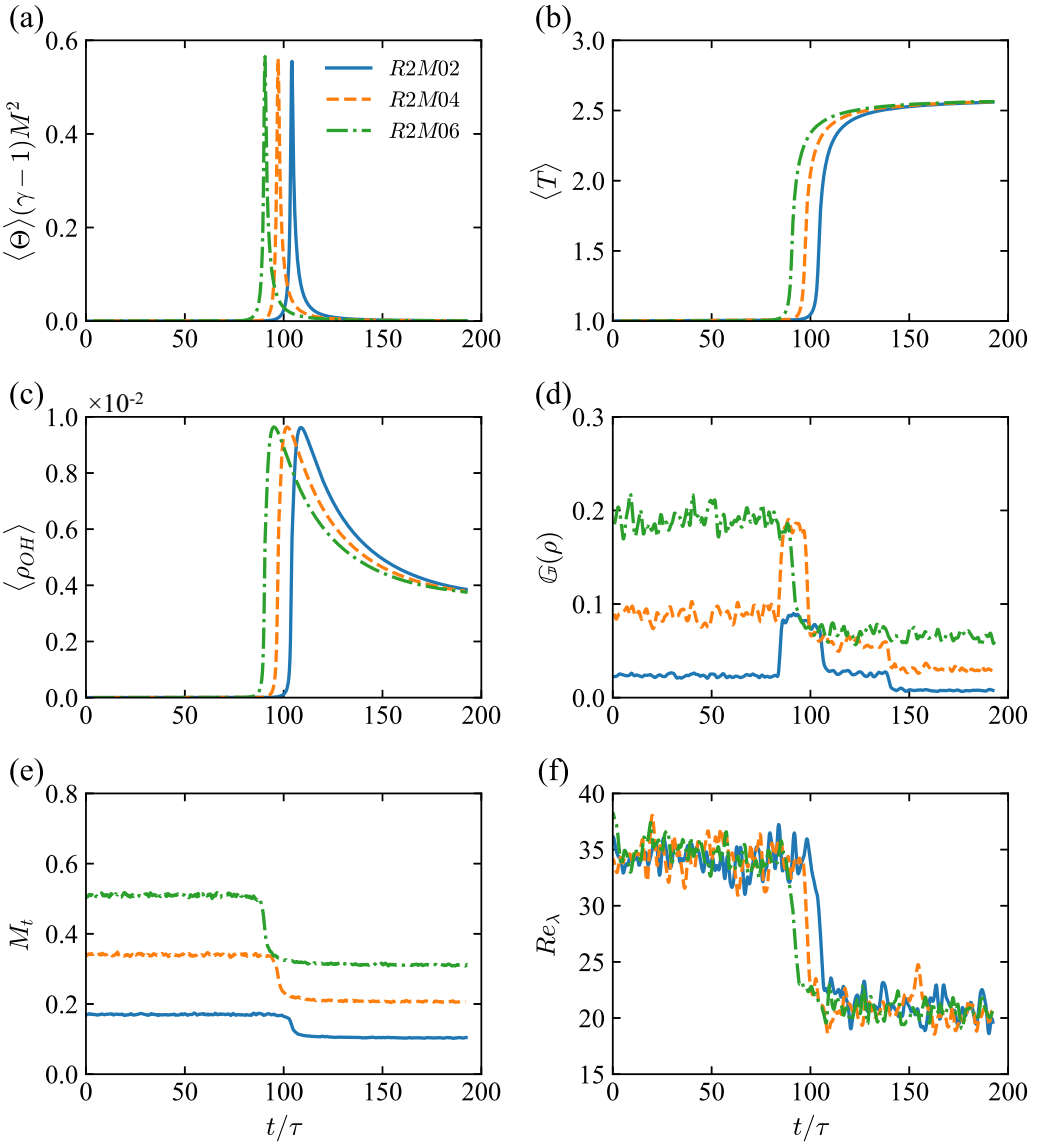

FIG. 23. Temporal variation of flow statistics of R2 at $M_{t,i} = 0.2, 0.4, 0.6$: (a) normalized averaged heat release $\langle\Theta\rangle(\gamma-1)M^2$; (b) averaged temperature $\langle T\rangle$; (c) averaged density of species OH $\langle\rho_{\mathrm{OH}}\rangle$; (d) averaged magnitude of density gradient $\mathbb{G}(\rho)$; (e) turbulent Mach number M_t; (f) Taylor Reynolds number Re_λ.

species $-H_s^0$, reaction rate of sth species $\dot{\omega}_s$, molecular weight of sth species $\mathbb{M}_s$, mean molecular weight of the mixture $\mathbb{M}$, specific heat at constant pressure of sth species $C_{p,s}$, specific heat at constant pressure of the mixture C_p, specific heat at constant volume of sth species $C_{v,s}$, and specific heat at constant volume of the mixture C_v. The specific heat at constant pressure of sth species $C_{p,s}$ can be obtained through polynomial fitting with Eq. (A6), in which the fitting coefficients $\zeta_{0,s}$, $\zeta_{1,s}$, $\zeta_{2,s}$, $\zeta_{3,s}$, and $\zeta_{4,s}$ can be found in [68].

We choose a detailed H_2/O_2 chemical reaction kinetics in the current study instead of a single-step chemistry previously used [35] based on two considerations. First, we want to improve our code in solving real combustion problems. Hydrogen/air combustion is important and widely considered

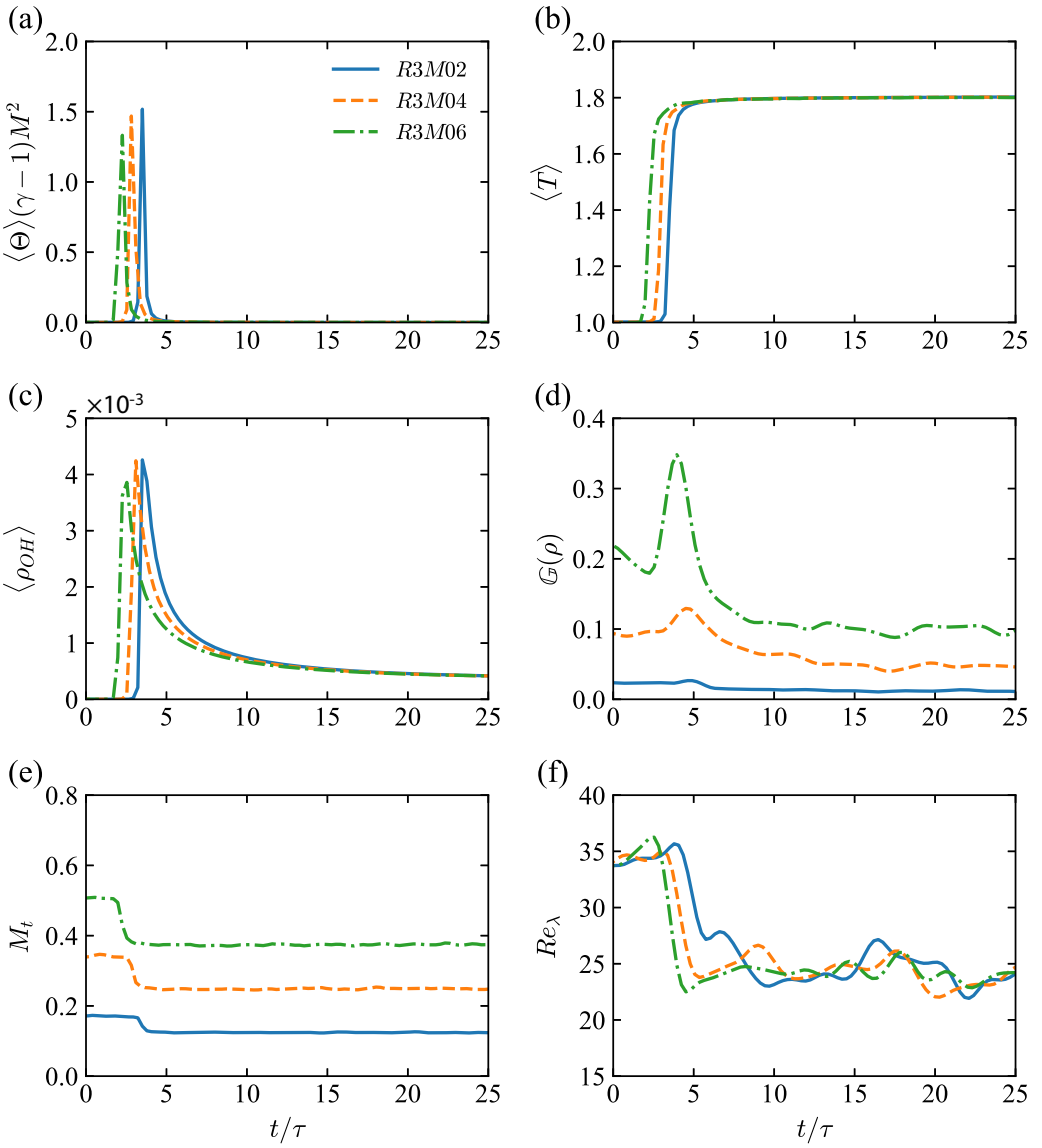

FIG. 24. Temporal variation of flow statistics of R3 at $M_{t,i} = 0.2, 0.4, 0.6$: (a) normalized averaged heat release $\langle\Theta\rangle(\gamma-1)M^2$; (b) averaged temperature $\langle T\rangle$; (c) averaged density of species OH $\langle\rho_{\mathrm{OH}}\rangle$; (d) averaged magnitude of density gradient $\mathbb{G}(\rho)$; (e) turbulent Mach number M_t; (f) Taylor Reynolds number Re_λ.

in clean energy utilization problems. Second, in previously used single-step chemistry, $\mathrm{Pr} = Sc = 0.7$, which suggested a unity Lewis number for all species. In current study, we consider a nonunity Lewis number situations for different species.

The experimental data from a H_2/O_2 reaction in a flow reactor by Mueller *et. al* [69] are used to validate the chemical reaction modeling. Table VII shows initial conditions for four validation cases. The initial mole fractions of H_2, O_2, and N_2 are given in the table, and the concentrations of six other species in the mixture are specified as 0.0. Figure 21 shows the comparison of zero-dimensional model results and experimental data. It is shown that the temporal variation of mole fraction of species H_2, H_2O, and O_2 in four cases collapses with the experimental data. The temporal variation

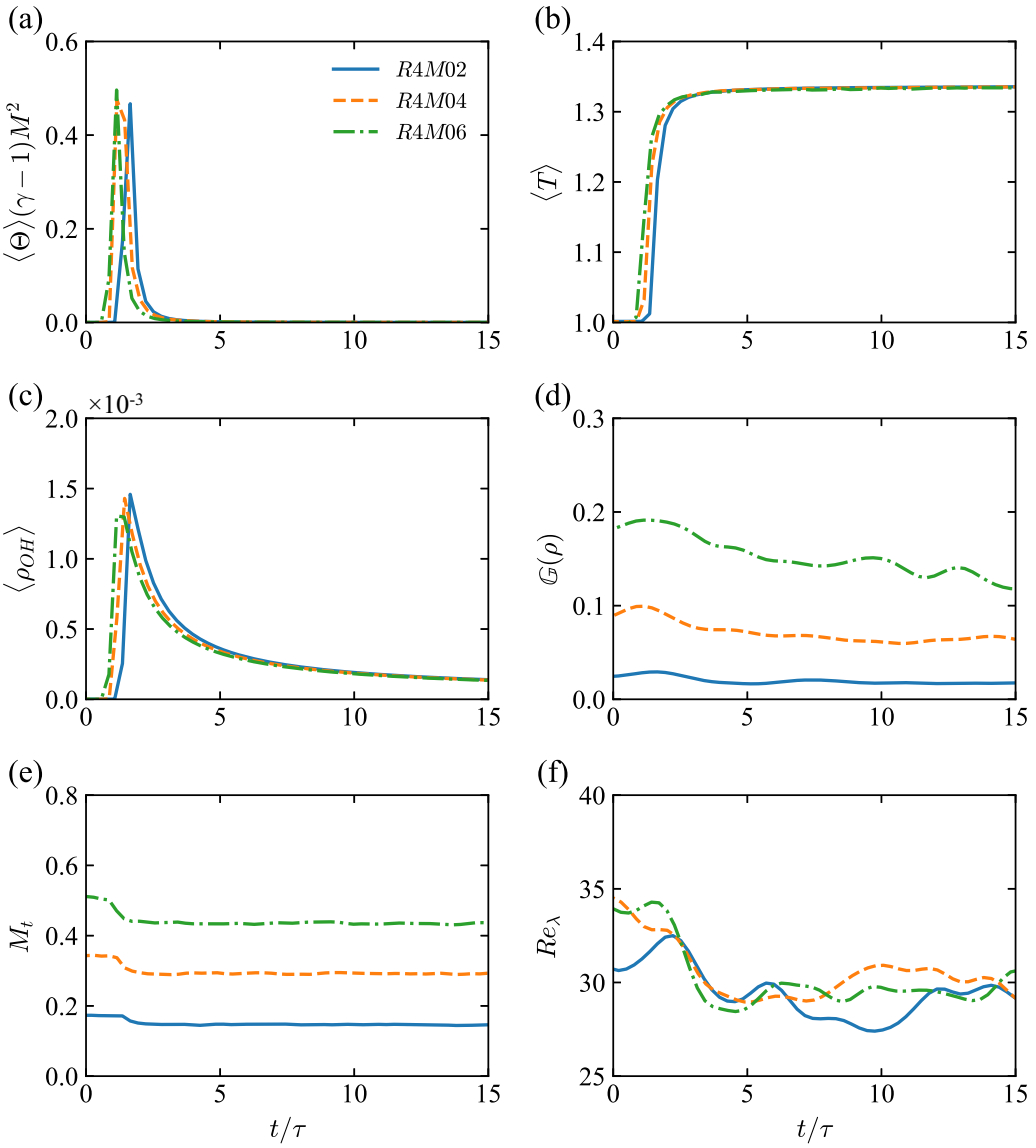

FIG. 25. Temporal variation of flow statistics of R4 at $M_{t,i} = 0.2, 0.4, 0.6$: (a) normalized averaged heat release $\langle\Theta\rangle(\gamma-1)M^2$; (b) averaged temperature $\langle T\rangle$; (c) averaged density of species OH $\langle\rho_{\mathrm{OH}}\rangle$; (d) averaged magnitude of density gradient $\mathbb{G}(\rho)$; (e) turbulent Mach number M_t; (f) Taylor Reynolds number Re_λ.

of temperature in case S13 and case S16 from the zero-dimensional model prediction is larger than experimental data at the later stage of chemical reaction. This deviation might result from that in the zero-dimensional chemical reaction model; kinetic energy is not considered, and thus the chemical reaction heat release has been completely converted to internal energy, leading to a larger spatially averaged temperature than experimental measurements in an actual environment. In general, the model predictions are in good agreement with the experimental data for different initial conditions.

We use nonunity Lewis numbers in current simulations and do not simulate the H_2/O_2 combustion under unity Lewis number situations for comparison. The effects of differential diffusion would be considered in future explorations. Lapointe *et al*. [70] studied the differential diffusion effects in

TABLE IX. Resulting flow statistics at reaction initial and end phases.

Case No.	$\mathrm{Re}_{\lambda,i}$	$\mathrm{Re}_{\lambda,e}$	$M_{t,i}$	$M_{t,e}$	$(\eta/\Delta x)_i$	$(\eta/\Delta x)_e$	$(L_I/\eta)_i$	$(L_I/\eta)_e$	Ka_i	Ka_e
R1M02	34	21	0.17	0.11	1.02	1.52	18.7	13.2	55	416
R1M04	34	21	0.34	0.21	1.03	1.52	18.8	13.2	35	54
R1M06	34	21	0.51	0.32	1.03	1.53	18.8	13.1	32	42
R2M02	34	21	0.17	0.10	1.03	1.56	18.8	12.9	185	3542
R2M04	34	21	0.34	0.21	1.03	1.56	18.8	12.9	250	643
R2M06	34	21	0.51	0.31	1.03	1.56	18.8	12.9	251	336
R3M02	34	25	0.17	0.12	1.01	1.33	18.9	14.8	991	1076
R3M04	34	25	0.34	0.25	1.02	1.36	18.8	14.6	567	1032
R3M06	34	25	0.51	0.37	1.03	1.36	18.8	14.6	140	629
R4M02	34	30	0.17	0.15	1.02	1.18	18.9	16.6	471	2795
R4M04	34	30	0.34	0.28	1.03	1.19	18.9	16.6	171	1301
R4M06	34	27	0.51	0.44	1.03	1.21	18.8	16.5	110	475

premixed n-heptane/air flames at different Karlovitz numbers using direct numerical simulations. They found that simulations with nonunity Lewis numbers exhibit lower mean fuel consumption and heat release rates than their unity Lewis number counterparts. However, the effects of differential diffusion decrease at large Karlovitz number situations. In our simulations for 128^3 and 256^3 grid resolutions, the Karlovitz numbers are larger than 100. Based on the findings by Lapointe *et al*., we expect that the differential diffusion effects would not be evident at large Taylor Reynolds numbers.

APPENDIX B: INFLUENCE OF INITIAL CONDITIONS

In order to enhance the general applicability of the present methods and results for H_2/O_2 reaction in compressible turbulence over a wide range of initial conditions, we provide the statistics of additional DNS data using 64^3 grid for different initial pressure, temperature, and species mass fractions.

1. Specification of DNS parameters

The specification of initial conditions for four reactions are provided in Table VIII. The initial conditions for reaction R1 are those adopted in the main text. The initial conditions for reactions R2–R4 are additional cases for comparison. For the four reactions, the mole fraction range of H_2 is 5%–16%, the mole fraction range of O_2 is 5%–40%, the initial temperature range is 880–1200 K, and the initial pressure range is 32 424–202 650 Pa.

2. Temporal variations of the flow statistics

Figures 22–25 show the temporal variations of flow statistics for the four reactions. It is observed that the temporal variations of flow statistics for reactions R2–R4 are similar to those for reaction R1. For the four reactions, with the increase of reaction heat release, the temperature increases, and the turbulent Mach number as well as the Taylor Reynolds number decreases. The initial conditions influence the time to reach the maximum heat release, the final averaged temperature, and the extent for the decrease of the turbulent Mach number and Taylor Reynolds number.

3. Averaged values of flow statistics

We provide the averaged values of flow statistics for different reaction phases in Tables IX and X. It is shown that the initial conditions influence the amount of heat release which result in a different

TABLE X. Resulting flow statistics at reaction initial and strong heat release phases.

Case No.	$S_{3,i}$	$S_{3,s}$	θ_i'	θ_s'	ω_i'	ω_s'	$(\theta'/\omega')_i$	$(\theta'/\omega')_s$	$(S'/\omega')_i$	$(S'/\omega')_s$
R1M02	−0.31	−0.30	0.02	0.01	3.86	3.35	0.006	0.003	0.707	0.707
R1M04	−0.33	−0.28	0.08	0.03	3.81	3.24	0.021	0.009	0.707	0.707
R1M06	−0.33	−0.21	0.24	0.14	3.85	3.22	0.061	0.043	0.710	0.709
R2M02	−0.33	−0.30	0.02	0.05	3.86	4.00	0.005	0.013	0.707	0.707
R2M04	−0.33	−0.36	0.08	0.11	3.81	3.81	0.021	0.029	0.709	0.707
R2M06	−0.31	−0.33	0.22	0.21	3.83	3.72	0.057	0.056	0.710	0.708
R3M02	−0.26	−0.27	0.02	0.15	3.95	3.38	0.005	0.044	0.707	0.707
R3M04	−0.30	−0.28	0.09	0.72	3.90	3.22	0.023	0.224	0.707	0.707
R3M06	−0.34	−0.58	0.23	1.07	3.88	3.20	0.059	0.334	0.710	0.708
R4M02	−0.36	−0.32	0.02	0.07	3.98	3.88	0.005	0.018	0.707	0.707
R4M04	−0.36	−0.29	0.08	0.25	3.92	3.82	0.020	0.065	0.707	0.707
R4M06	−0.33	−0.45	0.24	0.59	3.81	3.45	0.063	0.171	0.709	0.708

turbulent Mach number and Taylor Reynolds number in the reaction end phase. The variations of the averaged flow statistics for four reactions are similar to each other.

[1] M. S. Chong, A. E. Perry, and B. J. Cantwell, A general classification of three-dimensional flow fields, Phys. Fluids **2**, 765 (1990).

[2] J. Soria, R. Sondergaard, B. J. Cantwell, M. S. Chong, and A. E. Perry, A study of the fine-scale motions of incompressible time-developing mixing layers, Phys. Fluids **6**, 871 (1994).

[3] M. S. Chong, J. Soria, A. E. Perry, J. Chacin, B. J. Cantwell, and Y. Na, Turbulence structures of wall-bounded shear flows found using DNS data, J. Fluid Mech. **357**, 225 (1998).

[4] A. Ooi, J. Martin, J. Soria, and M. S. Chong, A study of the evolution and characteristics of the invariants of the velocity-gradient tensor in isotropic turbulence, J. Fluid Mech. **381**, 141 (1999).

[5] J. M. Wallace, Twenty years of experimental and direct numerical simulation access to the velocity gradient tensor: What have we learned about turbulence? Phys. Fluids **21**, 021301 (2009).

[6] C. Meneveau, Lagrangian dynamics and models of the velocity gradient tensor in turbulent flows, Annu. Rev. Fluid Mech. **43**, 219 (2011).

[7] R. Samtaney, D. I. Pullin, and B. Kosović, Direct numerical simulation of decaying compressible turbulence and shocklet statistics, Phys. Fluids **13**, 1415 (2001).

[8] S. Pirozzoli and F. Grasso, Direct numerical simulations of isotropic compressible turbulence: Influence of compressibility on dynamics and structures, Phys. Fluids **16**, 4386 (2004).

[9] D. A. Donzis and A. F. Maqui, Statistically steady states of forced isotropic turbulence in thermal equilibrium and non-equilibrium, J. Fluid Mech. **797**, 181 (2016).

[10] M. Danish, S. Suman, and S. S. Girimaji, Influence of flow topology and dilatation on scalar mixing in compressible turbulence, J. Fluid Mech. **793**, 633 (2016).

[11] J. Wang, T. Gotoh, and T. Watanabe, Shocklet statistics in compressible isotropic turbulence, Phys. Rev. Fluids **2**, 023401 (2017).

[12] J. Wang, M. Wan, S. Chen, C. Xie, and S. Chen, Effect of shock waves on the statistics and scaling in compressible isotropic turbulence, Phys. Rev. E **97**, 043108 (2018).

[13] D. A. Donzis and J. P. John, Universality and scaling in homogeneous compressible turbulence, Phys. Rev. Fluids **5**, 084609 (2020).

[14] D. A. Donzis, P. K. Yeung, and K. R. Sreenivasan, Dissipation and enstrophy in isotropic turbulence: Resolution effects and scaling in direct numerical simulations, Phys. Fluids **20**, 045108 (2008).

[15] G. I. Taylor, Production and dissipation of vorticity in a turbulent fluid, Proc. R. Soc. London A **164**, 15 (1938).
[16] S. B. Pope, *Turbulent Flows* (Cambridge University Press, Cambridge, 2000).
[17] R. Betchov, An inequality concerning the production of vorticity in isotropic turbulence, J. Fluid Mech. **1**, 497 (1956).
[18] W. T. Ashurst, A. R. Kerstein, R. M. Kerr, and C. H. Gibson, Alignment of vorticity and scalar gradient with strain rate in simulated Navier-Stokes turbulence, Phys. Fluids **30**, 2343 (1987).
[19] O. R. H. Buxton and B. Ganapathisubramani, Amplification of enstrophy in the far field of an axisymmetric turbulent jet, J. Fluid Mech. **651**, 483 (2010).
[20] Y. Zhou, K. Nagata, Y. Sakai, Y. Ito, and T. Hayase, Enstrophy production and dissipation in developing grid-generated turbulence, Phys. Fluids **28**, 025113 (2016).
[21] J. Wang, M. Wan, S. Chen, C. Xie, Q. Zheng, L.-P. Wang, and S. Chen, Effect of flow topology on the kinetic energy flux in compressible isotropic turbulence, J. Fluid Mech. **883**, A11 (2020).
[22] T. Arkady, *An Informal Conceptual Introduction to Turbulence*, 2nd ed. (Springer, Dordrecht, 2009)
[23] P. Bechlars and R. D. Sandberg, Variation of enstrophy production and strain rotation relation in a turbulent boundary layer, J. Fluid Mech. **812**, 321 (2017).
[24] L. Wang and X.-Y. Lu, Flow topology in compressible turbulent boundary layer, J. Fluid Mech. **703**, 255 (2012).
[25] P. E. Hamlington, A. Y. Poludnenko, and E. S. Oran, Intermittency in premixed turbulent reacting flows, Phys. Fluids **24**, 075111 (2012).
[26] V. Papapostolou, D. H. Wacks, N. Chakraborty, M. Klein, and H. G. Im, Enstrophy transport conditional on local flow topologies in different regimes of premixed turbulent combustion, Sci. Rep. **7**, 11545 (2017).
[27] M. Tanahashi, M. Fujimura, and T. Miyauchi, Coherent fine-scale eddies in turbulent premixed flames, Proce. Combust. Inst. **28**, 529 (2000).
[28] L. Cifuentes, C. Dopazo, J. Martín, P. Domingo, and L. Vervisch, Effects of the local flow topologies upon the structure of a premixed methane-air turbulent jet flame, Flow, Turbul. Combust. **96**, 535 (2016).
[29] D. H. Wacks, N. Chakraborty, M. Klein, P. G. Arias, and H. G. Im, Flow topologies in different regimes of premixed turbulent combustion: A direct numerical simulation analysis, Phys. Rev. Fluids **1**, 083401 (2016).
[30] J. Wang, Y. Shi, L.-P. Wang, Z. Xiao, X. T. He, and S. Chen, Effect of compressibility on the small-scale structures in isotropic turbulence, J. Fluid Mech. **713**, 588 (2012).
[31] N. Chakraborty, Statistics of vorticity alignment with local strain rates in turbulent premixed flames, Eur. J. Mech. B Fluids **46**, 201 (2014).
[32] A. Kazbekov, K. Kumashiro, and A. M. Steinberg, Enstrophy transport in swirl combustion, J. Fluid Mech. **876**, 715 (2019).
[33] J. J. Doom, Direct numerical simulation of turbulent, chemically reacting flows, Ph.D. thesis, University of Minnesota (2009).
[34] R. Jahanbakhshi, DNS of compressible reacting turbulent shear layer, Ph.D. thesis, State University of New York at Buffalo (2016).
[35] J. Teng, J. Wang, H. Li, and S. Chen, Spectra and scaling in chemically reacting compressible isotropic turbulence, Phys. Rev. Fluids **5**, 084601 (2020).
[36] C. Qian, W. Bing, Z. Huiqiang, Z. Yunlong, and G. Wei, Numerical investigation of H_2/air combustion instability driven by large scale vortex in supersonic mixing layers, Int. J. Hydrogen Energy **41**, 3171 (2016).
[37] J. Wang, L.-P. Wang, Z. Xiao, Y. Shi, and S. Chen, A hybrid numerical simulation of isotropic compressible turbulence, J. Comput. Phys. **229**, 5257 (2010).
[38] J. Wang, Y. Shi, L.-P. Wang, Z. Xiao, X. T. He, and S. Chen, Scaling and Statistics in Three-Dimensional Compressible Turbulence, Phys. Rev. Lett. **108**, 214505 (2012).
[39] S. Jagannathan and D. A. Donzis, Reynolds and mach number scaling in solenoidally-forced compressible turbulence using high-resolution direct numerical simulations, J. Fluid Mech. **789**, 669 (2016).
[40] J. Wang, M. Wan, S. Chen, and S. Chen, Kinetic energy transfer in compressible isotropic turbulence, J. Fluid Mech. **841**, 581 (2018).

[41] S. Chen and N. Cao, Anomalous Scaling and Structure Instability in Three-Dimensional Passive Scalar Turbulence, Phys. Rev. Lett. **78**, 3459 (1997).
[42] J. Li, Z. Zhao, A. Kazakov, and F. L. Dryer, An updated comprehensive kinetic model of hydrogen combustion, Int. J. Chem. Kinet. **36**, 566 (2004).
[43] H. Im, J. Chen, and C. Law, Ignition of hydrogen-air mixing layer in turbulent flows, Symp. (Intl.) Combust. **27**, 1047 (1998).
[44] S. K. Lele, Compact finite difference schemes with spectral-like resolution, J. Comput. Phys. **103**, 16 (1992).
[45] D. S. Balsara and C.-W. Shu, Monotonicity preserving weighted essentially non-oscillatory schemes with increasingly high order of accuracy, J. Comput. Phys. **160**, 405 (2000).
[46] W.-G. Zhao, H.-W. Zheng, F.-J. Liu, X.-T. Shi, J. Gao, N. Hu, M. Lv, S.-C. Chen, and H.-D. Zhao, An efficient unstructured WENO method for supersonic reactive flows, Acta Mech. Sin. **34**, 623 (2018).
[47] J. Wang, Y. Shi, L.-P. Wang, Z. Xiao, X. He, and S. Chen, Effect of shocklets on the velocity gradients in highly compressible isotropic turbulence, Phys. Fluids **23**, 125103 (2011).
[48] X. Chen, G. Dong, and B. Li, Numerical study of three-dimensional developments of premixed flame induced by multiple shock waves, Acta Mech. Sin. **34**, 1035 (2018).
[49] J. Wang, Y. Yang, Y. Shi, Z. Xiao, X. T. He, and S. Chen, Cascade of Kinetic Energy in Three-Dimensional Compressible Turbulence, Phys. Rev. Lett. **110**, 214505 (2013).
[50] J. Wang, Y. Yang, Y. Shi, Z. Xiao, X. T. He, and S. Chen, Statistics and structures of pressure and density in compressible isotropic turbulence, J. Turbul. **14**, 21 (2013).
[51] X. Wang, J. Wang, H. Li, and S. Chen, Kinetic energy transfer in compressible homogeneous anisotropic turbulence, Phys. Rev. Fluids **6**, 064601 (2021).
[52] D. Xu, J. Wang, M. Wan, C. Yu, X. Li, and S. Chen, Compressibility effect in hypersonic boundary layer with isothermal wall condition, Phys. Rev. Fluids **6**, 054609 (2021).
[53] Z. Zhao, Z. Chen, and S. Chen, Correlations for the ignition delay times of hydrogen/air mixtures, Chin. Sci. Bull. **56**, 215 (2011).
[54] K. Malik, M. Żbikowski, and A. Teodorczyk, Laminar burning velocity model based on deep neural network for hydrogen and propane with air, Energies **13**, 3381 (2020).
[55] J. Teng, J. Wang, H. Li, and S. Chen, Interscale kinetic energy transfer in chemically reacting compressible isotropic turbulence, J. Fluid Mech. **912**, A36 (2021).
[56] T. Watanabe and T. Gotoh, Inertial-range intermittency and accuracy of direct numerical simulation for turbulence and passive scalar turbulence, J. Fluid Mech. **590**, 117 (2007).
[57] J. Wang, T. Gotoh, and T. Watanabe, Spectra and statistics in compressible isotropic turbulence, Phys. Rev. Fluids **2**, 013403 (2017).
[58] H. Wang, E. R. Hawkes, J. H. Chen, B. Zhou, Z. Li, and M. Aldén, Direct numerical simulations of a high Karlovitz number laboratory premixed jet flame—An analysis of flame stretch and flame thickening, J. Fluid Mech. **815**, 511 (2017).
[59] P. Norbert, *Turbulent Combustion* (Cambridge University Press, Cambridge, 2004).
[60] G. Erlebacher and S. Sarkar, Statistical analysis of the rate of strain tensor in compressible homogeneous turbulence, Phys. Fluids **5**, 3240 (1993).
[61] K. Lee, S. S. Girimaji, and J. Kerimo, Effect of compressibility on turbulent velocity gradients and small-scale structure, J. Turbul. **10**, N9 (2009).
[62] W. Han, A. Scholtissek, F. Dietzsch, R. Jahanbakhshi, and C. Hasse, Influence of flow topology and scalar structure on flame-tangential diffusion in turbulent non-premixed combustion, Combust. Flame **206**, 21 (2019).
[63] C. B. da Silva and J. C. F. Pereira, Invariants of the velocity-gradient, rate-of-strain, and rate-of-rotation tensors across the turbulent/nonturbulent interface in jets, Phys. Fluids **20**, 055101 (2008).
[64] M. I. Cheikh, J. Chen, and M. Wei, Small-scale energy cascade in homogeneous isotropic turbulence, Phys. Rev. Fluids **4**, 104610 (2019).
[65] S. Suman and S. S. Girimaji, Velocity gradient invariants and local flow-field topology in compressible turbulence, J. Turbul. **11**, N2 (2010).

[66] G. E. Elsinga and I. Marusic, Universal aspects of small-scale motions in turbulence, J. Fluid Mech. **662**, 514 (2010).

[67] J. Lai, D. H. Wacks, and N. Chakraborty, Flow topology distribution in head-on quenching of turbulent premixed flame: A direct numerical simulation analysis, Fuel **224**, 186 (2018).

[68] A. Burcat, Thermochemical data for combustion calculations, in *Combustion Chemistry*, edited by W. C. Gardiner (Springer, New York, 1984), pp. 455–473.

[69] M. A. Mueller, R. A. Yetter, and F. L. Dryer, Flow reactor studies and kinetic modeling of the $H_2/O_2/NO_X$ and $CO/H_2O/O_2/NO_X$ reactions, Int. J. Chem. Kinet. **31**, 705 (1999).

[70] S. Lapointe, B. Savard, and G. Blanquart, Differential diffusion effects, distributed burning, and local extinctions in high Karlovitz premixed flames, Combust. Flame **162**, 3341 (2015).